Check for updates

FIBROSIS

Copyright © 2023 The Authors, some rights reserved; exclusive licensee American Association for the Advancement of Science. No claim to original U.S. Government Works

Identification of a broadly fibrogenic macrophage subset induced by type 3 inflammation

Thomas Fabre[1]*†, Alexander M. S. Barron[1]†, Stephen M. Christensen[1], Shoh Asano[1], Kathryn Bound[1], Matthew P. Lech[1], Marc H. Wadsworth II[1], Xiao Chen[1], Chang Wang[1], Ju Wang[1], James McMahon[1], Franklin Schlerman[1], Alexis White[1], Kellie M. Kravarik[1], Andrew J. Fisher[2], Lee A. Borthwick[3], Kevin M. Hart[1], Neil C. Henderson[4,5], Thomas A. Wynn[1]†, Ken Dower[1]†

Macrophages are central orchestrators of the tissue response to injury, with distinct macrophage activation states playing key roles in fibrosis progression and resolution. Identifying key macrophage populations found in human fibrotic tissues could lead to new treatments for fibrosis. Here, we used human liver and lung single-cell RNA sequencing datasets to identify a subset of *CD9*$^+$*TREM2*$^+$ macrophages that express *SPP1*, *GPNMB*, *FABP5*, and *CD63*. In both human and murine hepatic and pulmonary fibrosis, these macrophages were enriched at the outside edges of scarring and adjacent to activated mesenchymal cells. Neutrophils expressing MMP9, which participates in the activation of TGF-β1, and the type 3 cytokines GM-CSF and IL-17A coclustered with these macrophages. In vitro, GM-CSF, IL-17A, and TGF-β1 drive the differentiation of human monocytes into macrophages expressing scar-associated markers. Such differentiated cells could degrade collagen IV but not collagen I and promote TGF-β1–induced collagen I deposition by activated mesenchymal cells. In murine models blocking GM-CSF, IL-17A or TGF-β1 reduced scar-associated macrophage expansion and hepatic or pulmonary fibrosis. Our work identifies a highly specific macrophage population to which we assign a profibrotic role across species and tissues. It further provides a strategy for unbiased discovery, triage, and preclinical validation of therapeutic targets based on this fibrogenic macrophage population.

INTRODUCTION

Organ fibrosis represents a major cause of morbidity and mortality worldwide (*1*). Fibrosis can arise from multiple etiologies and affect virtually any organ (*2*). Prominent among fibrotic diseases are nonalcoholic steatohepatitis (NASH), the fastest growing cause of liver fibrosis (*3*), and idiopathic pulmonary fibrosis (IPF), the prototypical progressive-fibrosing interstitial lung disease (*4*). In both diseases, inflammation shapes the interactions and phenotypes of cells within the fibrotic niche (*1*, *3*, *5*–*9*). However, how much of this cellular dialogue is organ, disease, or species specific remains unclear (*3*, *5*, *6*).

Macrophages are critical effector cells in both fibrosis progression and resolution (*7*, *10*). Recent data have revealed "scar-associated macrophages" (SAMs) expressing TREM2 and/or CD9 in hepatic and pulmonary fibrosis (*11*–*21*). *CD9*$^+$*TREM2*$^+$ macrophages are also associated with Alzheimer's disease, obese adipose tissue, and atherosclerotic lesions, suggesting that these markers are expressed by several myeloid populations with potentially nonoverlapping functions (*21*–*24*). SAMs likely originate from monocytes, localize to the scar, and induce myofibroblast activation in response to niche and inflammatory signals that influence their differentiation and function (*7*, *10*–*12*, *15*, *25*–*27*). Fibrosis-associated inflammation can vary, but in NASH and IPF, it is characterized by a mixture of type 1, 2, and 3 cytokines (*1*, *8*, *9*). Outstanding questions in the field of fibrosis are the precise definition of the SAM population, the cellular and molecular drivers of their differentiation, and insights into their function in the fibrotic niche.

To address this, we used human single-cell RNA sequencing (scRNA-seq) data and murine models of lung and liver fibrosis to identify a core SAM phenotype. These SAMs are a subset of *CD9*$^+$*TREM2*$^+$ macrophages that express SPP1, GPNMB, FABP5, and CD63 and are enriched in human and murine hepatic and pulmonary fibrosis. RNA velocity suggested that they originate from infiltrating monocytes and represent an intermediate differentiation state. Tissue mapping revealed that these SAMs were enriched in scars and colocated with myofibroblasts and IL-17$^+$GM-CSF$^+$ MMP9$^+$ neutrophils, forming a deleterious trifecta of cell types that express a variety of profibrotic mediators. In vitro, interleukin-17A (IL-17A), granulocyte-macrophage colony-stimulating factor (GM-CSF), and transforming growth factor–β (TGF-β) drove the differentiation of human monocytes into macrophages expressing SAM markers. Such in vitro–differentiated cells could degrade basement membrane collagen type IV but not collagen type I and promoted collagen type I deposition by activated mesenchymal cells in coculture. In vivo, blocking IL-17A, GM-CSF, or TGF-β reduced both SAM accumulation and fibrosis severity in several murine models of organ fibrosis. Together, with high precision and using orthogonal techniques, we have identified a cross-species, cross-organ SAM population and provided insights into their origin and roles in the fibrotic niche. Targeting the cells or their differentiation or function represents promising pan-antifibrotic strategies.

[1]Pfizer Inc., Cambridge, MA, USA. [2]Translational and Clinical Research Institute, Faculty of Medical Sciences, Newcastle University, Newcastle upon Tyne, UK. [3]Newcastle Fibrosis Research Group, Biosciences Institute, Newcastle University, Newcastle upon Tyne, UK. [4]MRC Human Genetics Unit, Institute of Genetics and Cancer, University of Edinburgh, Edinburgh, UK. [5]Centre for Inflammation Research, the Queen's Medical Research Institute, University of Edinburgh, Edinburgh, UK.
*Corresponding author. Email: thomas.fabre@pfizer.com
†These authors contributed equally to this work.

Downloaded from https://www.science.org at Tsinghua University on October 24, 2025

RESULTS

Integration of human scRNA-seq datasets identifies a cross-tissue SAM subset

We integrated nine public scRNA-seq datasets for characterization of macrophage populations broadly associated with fibrosis. These included liver (44 healthy and 5 cirrhotic patients from five studies) and lung datasets (51 healthy and 66 fibrotic patients from four studies). Fibrotic etiologies for liver were alcoholic liver disease (n = 2), nonalcoholic fatty liver disease (n = 2), and primary biliary cholangitis (n = 1); for lung, they were systemic sclerosis interstitial lung disease (n = 10) and IPF (n = 56). Quality control–based filtering, normalization, and integration (for details, see Materials and Methods) created liver and lung atlases composed of 328,783 (ID SCP2154, https://singlecell.broadinstitute.org/single_cell/study/SCP2154/identification-of-a-broadly-fibrogenic-macrophage-subset-induced-by-type-3-inflammation-human-liver-fibrosis-scrnaseq-atlas) and 616,918 cells (ID SCP2155, https://singlecell.broadinstitute.org/single_cell/study/SCP2155/identification-of-a-broadly-fibrogenic-macrophage-subset-induced-by-type-3-inflammation-human-lung-fibrosis-scrnaseq-atlas), respectively (Fig. 1A and figs. S1 and S2). These atlases demonstrated altered proportions of multiple cell types, including myeloid cells (Fig. 1, B to G).

To characterize macrophage subsets associated with fibrosis, we integrated the liver and lung myeloid cells into a single atlas (Fig. 1, H to J, and fig. S3) composed of 167,856 cells: 37,575 from the liver and 130,281 from the lung (ID SCP2156, https://singlecell.broadinstitute.org/single_cell/study/SCP2156/identification-of-a-broadly-fibrogenic-macrophage-subset-induced-by-type-3-inflammation-human-liver-lung-myeloid-fibrosis-scrnaseq-atlas). We confirmed the biological validity of our integration by demonstrating that Kupffer cells and alveolar macrophages were restricted to the liver and lung, respectively (Fig. 1, K to M, and fig. S4). Our myeloid atlas approach recapitulated the previous finding that *CD9*$^+$*TREM2*$^+$ macrophages expand in human liver fibrosis, and we now reveal that a similar population is also expanded in human lung fibrosis (Fig. 1O and fig. S4). All three human atlases are available on the Broad Institute's Single Cell Portal.

SPP1, *GPNMB*, and *FABP5* resolve SAMs from a heterogeneous *CD9*$^+$*TREM2*$^+$ population

Analysis of *CD9* and *TREM2* expression within the myeloid atlas demonstrated that these markers identified multiple populations. The addition of SPP1 and/or CD63 was able to resolve the granularity within the *CD9*$^+$*TREM2*$^+$ population (Fig. 2A). For example, there was no increase in *CD9*$^+$*TREM2*$^+$*SPP1*$^-$ macrophages in liver fibrosis, whereas *CD9*$^+$*TREM2*$^+$*SPP1*$^+$ macrophages increased in both liver and lung fibrosis (Fig. 2, B and C). Curating the data, we identified that the combination of *SPP1* and *GPNMB* with *FABP5* or *CD63* had the best specificity for identifying SAM within the *CD9*$^+$*TREM*$^+$ population; this was independently confirmed by the unbiased tool COMET, which identifies gene markers for cell populations in scRNA-seq data (fig. S5).

We validated these findings at the protein level in situ using cyclic immunofluorescent (cycIF) and histologic staining of sections from fibrotic livers (eight F1–F2 NASH and nine F3–F4 NASH) and fibrotic lungs (six healthy and eight IPF). SPP1, GPNMB, and FABP5 were coexpressed in human NASH and IPF tissue (Fig. 2D), and picrosirius red (PSR) staining of serial sections demonstrated that IBA1$^+$ macrophages that were SPP1$^+$GPNMB$^+$FABP5$^+$ were enriched at the edges of red, PSR$^+$ collagen scars (Fig. 2E and fig. S6). SPP1$^+$ cells covered more area in cirrhotic F4 versus F1 NASH livers but not in IPF versus healthy lungs (Fig. 2F). Combining these three markers enhanced the differences between F4 and F1 livers and was required to identify the expansion in frequency and area covered by SAMs in IPF lungs (Fig. 2, G and H). Thus, the SPP1$^+$GPNMB$^+$FABP5$^+$ subpopulation is the most increased and scar-associated of the *CD9*$^+$*TREM2*$^+$ macrophages in human liver and lung fibrosis. We herein refer to these SAM as "Fab5," for five marker–positive SAMs.

Myeloid cells and neutrophils accumulate within and at the edge of the scar in murine liver fibrosis models

To determine whether a comparable population exists in mouse models of fibrosis, we analyzed livers from mice treated with carbon tetrachloride (CCl_4) or fed high-fat diet (HFD). We first confirmed that these mice developed robust fibrosis by PSR staining and hydroxyproline quantification (Fig. 3, A to D). Next, we performed scRNA-seq and integrated data from three CCl_4 and three HFD studies to generate a murine liver fibrosis atlas. After quality control and doublet filtering, the final atlas consisted of 84,973 cells (7971 olive oil, 6932 CCl_4, 26,327 chow, and 43,743 HFD) and is available on the Broad Institute's Single Cell Portal (ID SCP2053, https://singlecell.broadinstitute.org/single_cell/study/SCP2053/identification-of-a-broadly-fibrogenic-macrophage-subset-induced-by-type-3-inflammation-murine-liver-fibrosis-scrnaseq-atlas) (fig. S7). As seen in the human fibrosis atlases, murine liver fibrosis was accompanied by dysregulation of leukocyte populations, including myeloid cells (Fig. 3, E and F). This was confirmed by flow cytometry analysis (Fig. 3, G to P), which demonstrated an increase in Ly6C^{hi} monocytes and macrophages in both CCl_4 and HFD, and an increase in Ly6C^{lo} macrophages in CCl_4 but a decrease in HFD (fig. S8). Using cycIF, we also observed an increase in S100A8/A9$^+$ neutrophils that colocalized with Iba1$^+$ macrophages in CCl_4 and HFD livers; in addition, *Iba1*$^+$ macrophages converged on areas of fibrosis and steatosis in CCl_4 and HFD livers (Fig. 3, Q to S).

Murine Fab5 macrophages originate from monocytes based on their transcriptional trajectories and specifically accumulate in fibrotic lesions

When subclustering murine macrophages (10,841 cells: 428 olive oil, 3349 CCl_4, 2009 chow, and 5055 HFD) from these mouse models of liver fibrosis (ID SCP2164, https://singlecell.broadinstitute.org/single_cell/study/SCP2164/identification-of-a-broadly-fibrogenic-macrophage-subset-induced-by-type-3-inflammation-murine-liver-fibrosis-myeloid-scrnaseq-atlas), we were able to identify the Fab5 signature (Fig. 4A and fig. S9). Applying RNA velocity suggested that monocytes pass through an inflammatory macrophage state before acquiring the Fab5 phenotype, as seen previously with CD9$^+$TREM2$^+$ macrophages (Fig. 4, B to D) (*11*, *12*, *14*). To confirm that this population was associated with fibrosis progression, we performed flow cytometry using a surrogate gating strategy because of lack of flow reagents for murine SPP1 and FABP5. Manual curation and COMET demonstrated that the combination of *Trem2*, *Cd9*, *Cd63*, and *Gpnmb* was equally selective for this population (fig. S10). This combination of markers validated

Downloaded from https://www.science.org at Tsinghua University on October 24, 2025

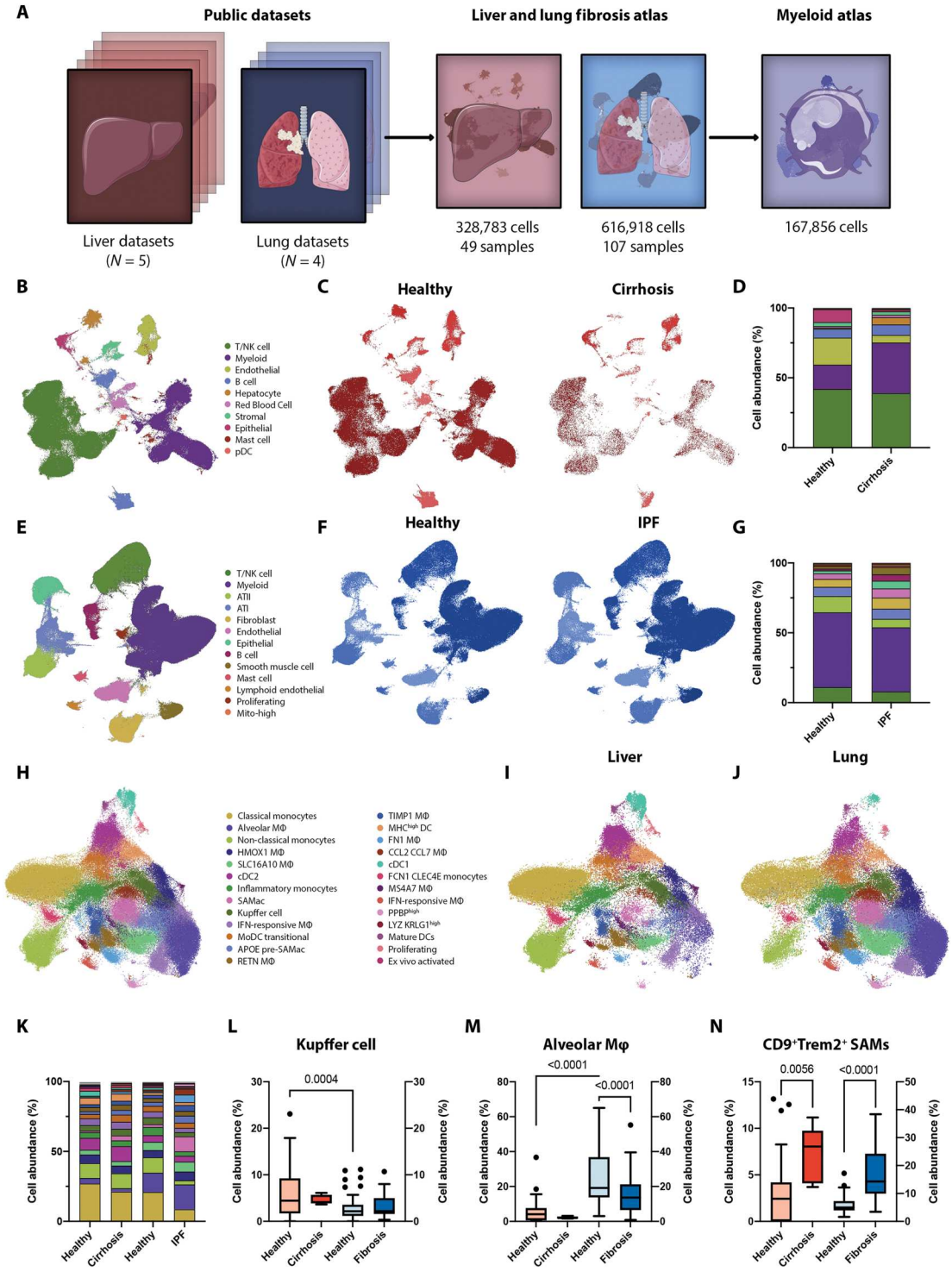

Fig. 1. Integration of human scRNA-seq lung and liver fibrosis datasets identified *CD9*$^{+}$*TREM2*$^{+}$ SAMs as cross-tissue SAMs. (**A**) Summary of the scRNA-seq atlas construction. (**B**) UMAP plot of all cells from integrated liver datasets colored by cell type. (**C**) UMAP plots of cells from healthy and cirrhotic livers shaded by cell type. (**D**) Stacked bar chart of liver cell subset frequencies. (**E**) UMAP plot of all cells from integrated lung datasets colored by cell type. (**F**) UMAP plots of cells from healthy and fibrotic lungs shaded by cell type. (**G**) Stacked bar chart of lung cell subset frequencies. (**H**) UMAP plot of myeloid atlas from integrated lung and liver datasets colored by subtype. (**I** and **J**) UMAP plots of myeloid cells from the liver and lung colored by subtype. (**K**) Stacked bar chart of simplified myeloid cell subset frequencies from liver and lungs. (**L** to **N**) Frequency per sample of Kupffer cells, alveolar macrophages, and *CD9*$^{+}$*TREM2*$^{+}$ SAMs in cirrhotic livers (red) and fibrotic lungs (blue). Left axis is frequency in liver; right axis is frequency in lung. Dots represent samples more than 1 SD from the mean. Statistics: Mann-Whitney *U* test, *P* values displayed on plots.

Downloaded from https://www.science.org at Tsinghua University on October 24, 2025

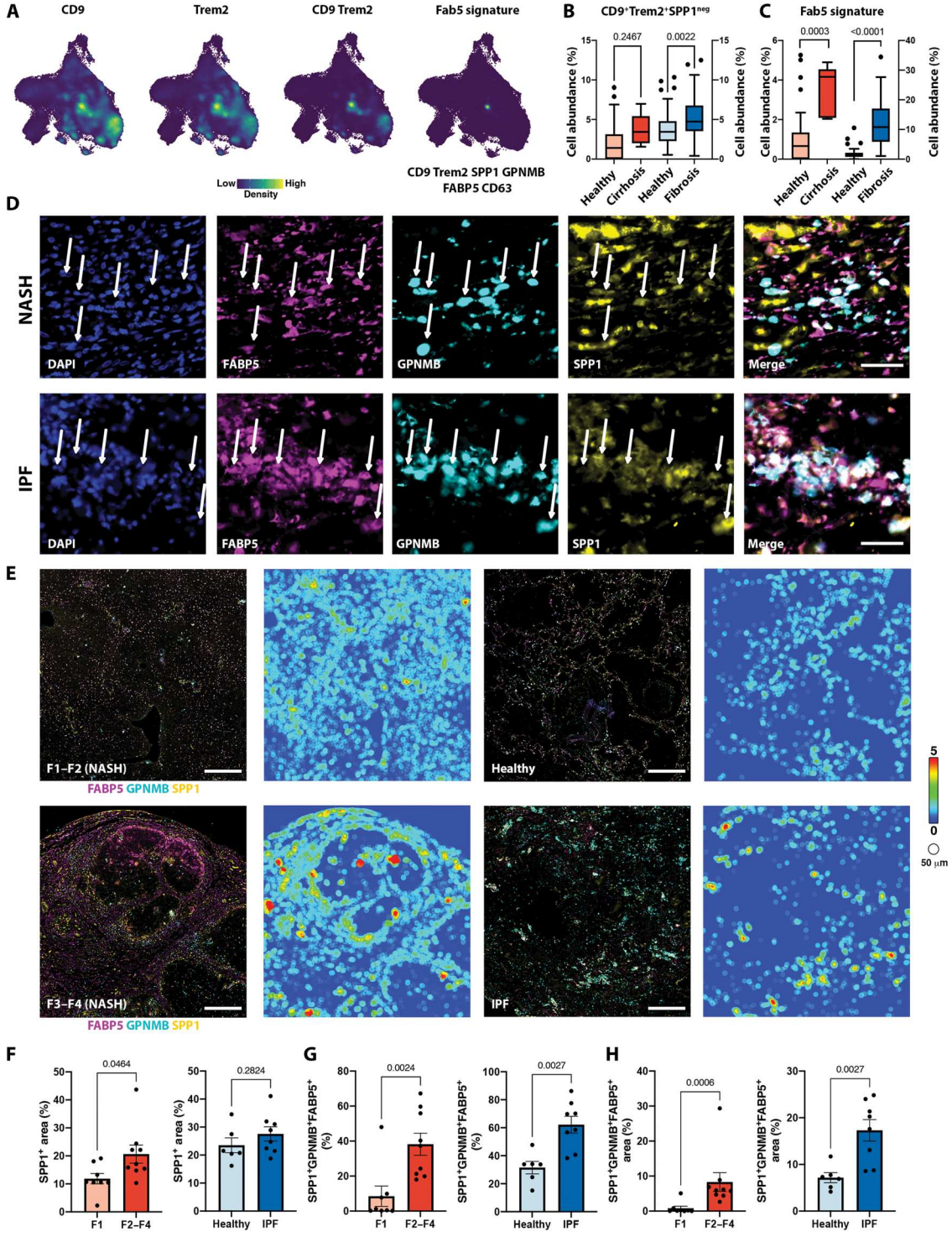

Fig. 2. CD9$^+$TREM2$^+$ macrophages in human liver and lung fibrotic disease are a heterogeneous population from which accumulating SAMs can be further resolved via coexpression of SPP1, GPNMB, CD63, and FABP5. (**A**) Nebulosa plots showing densities of CD9, TREM2, joint density of CD9 and TREM2, or joint density of the Fab5 signature (CD9, TREM2, SPP1, GPNMB, FABP5, and CD63) allowing precise identification of SAMs. (**B** and **C**) Frequency of CD9$^+$TREM2$^+$SPP1^{neg} and Fab5 SAMs in liver (red) and lung (blue). Left *y* axis is frequency in liver; right *y* axis is frequency in lung. (**D**) High-magnification cycIF of SPP1, GPNMB, and FABP5 in human F3–F4 NASH livers and IPF lungs. White arrows indicate cells coexpressing all three markers. Scale bars, 50 μm. (**E**) Low-magnification cycIF images (scale bars, 500 μm) as in (D) and accompanying tissue heatmaps (scale, blue = 0 to red = 5 cells per 50 μm) of SPP1$^+$ cells. (**F**) SPP1$^+$ area in liver (red) and lung (blue). (**G**) Frequencies of SPP1$^+$GPNMB$^+$ FABP5$^+$ cells in livers (red) and lungs (blue). (**H**) Areas of SPP1$^+$GPNMB$^+$FABP5$^+$ cells in livers (red) and lungs (blue). Statistics: Mann-Whitney *U* test, *P* values displayed on plots.

Downloaded from https://www.science.org at Tsinghua University on October 24, 2025

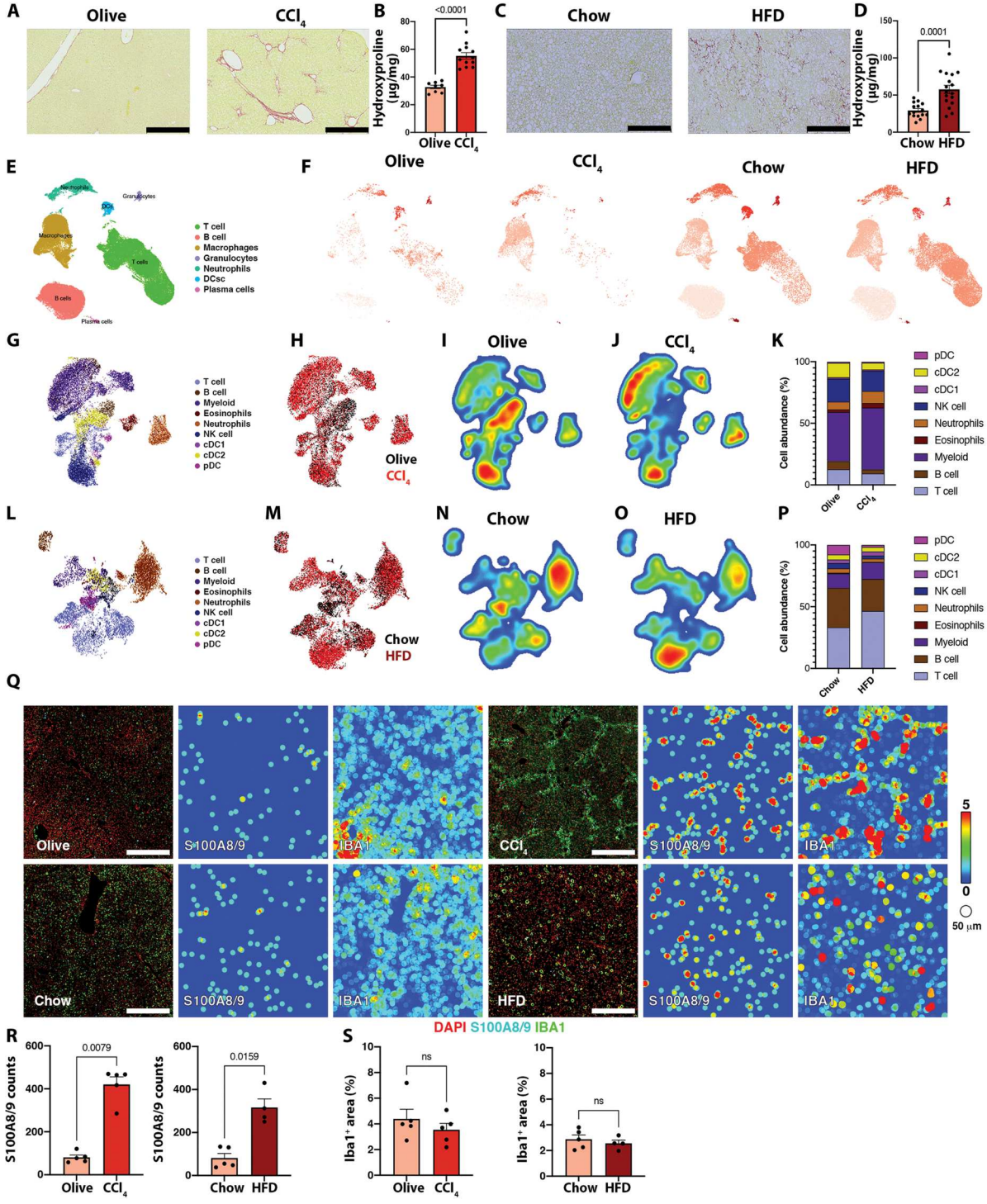

Fig. 3. Myeloid cells and neutrophils accumulate within and at the edge of the scar in murine liver fibrosis models. (**A**) Representative picro Sirius red staining of olive oil and CCl_4 livers. (**B**) Quantification of hydroxyproline content in CCl_4 injury. (**C**) Representative images of picro Sirius Red staining of chow and HFD livers. (**D**) Quantification of hydroxyproline content in HFD. (**E**) UMAP scRNA-seq plot of leukocytes from olive oil, CCl_4, chow, and HFD livers. (**F**) UMAP scRNA-seq plots of liver leukocytes split by condition and shaded by cell type. (**G** and **H**) UMAP FACS plot of $CD45^+$ cells from CCl_4 model colored by cell type (G) or by condition [olive oil (black) and CCl_4 (red), (H)]. (**I** and **J**) UMAP FACS density plots of $CD45^+$ cells in olive oil (I) and CCl_4 (J). Blue, lowest frequency; red, highest frequency. (**K**) Stacked bar chart of $CD45^+$ cell populations in CCl_4 injury. (**L** and **M**) UMAP FACS plots of $CD45^+$ cells from HFD model colored by cell type (L) or condition [chow (black) and HFD (dark red)] (M). (**N** and **O**) UMAP FACS density plots of $CD45^+$ cells in chow (N) and HFD (O) as in (I) and (J). (**P**) Stacked bar chart of $CD45^+$ cell populations in HFD. (**Q**) cycIF of S100A8/A9 (neutrophils) and Iba1 (macrophages) in olive oil, CCl_4, chow, and HFD. Representative tissue heatmaps (scale, blue = 0 to red = 5 cells per 50 µm) of S100A8/A9 and Iba1. (**R**) Increased numbers of $S100A8/A9^+$ neutrophils in CCl_4 and HFD models by cycIF. (**S**) $Iba1^+$ positive area by cycIF. Scale bars, 500 µm. Statistics: Mann-Whitney *U* test, *P* values displayed on plots.

Downloaded from https://www.science.org at Tsinghua University on October 24, 2025

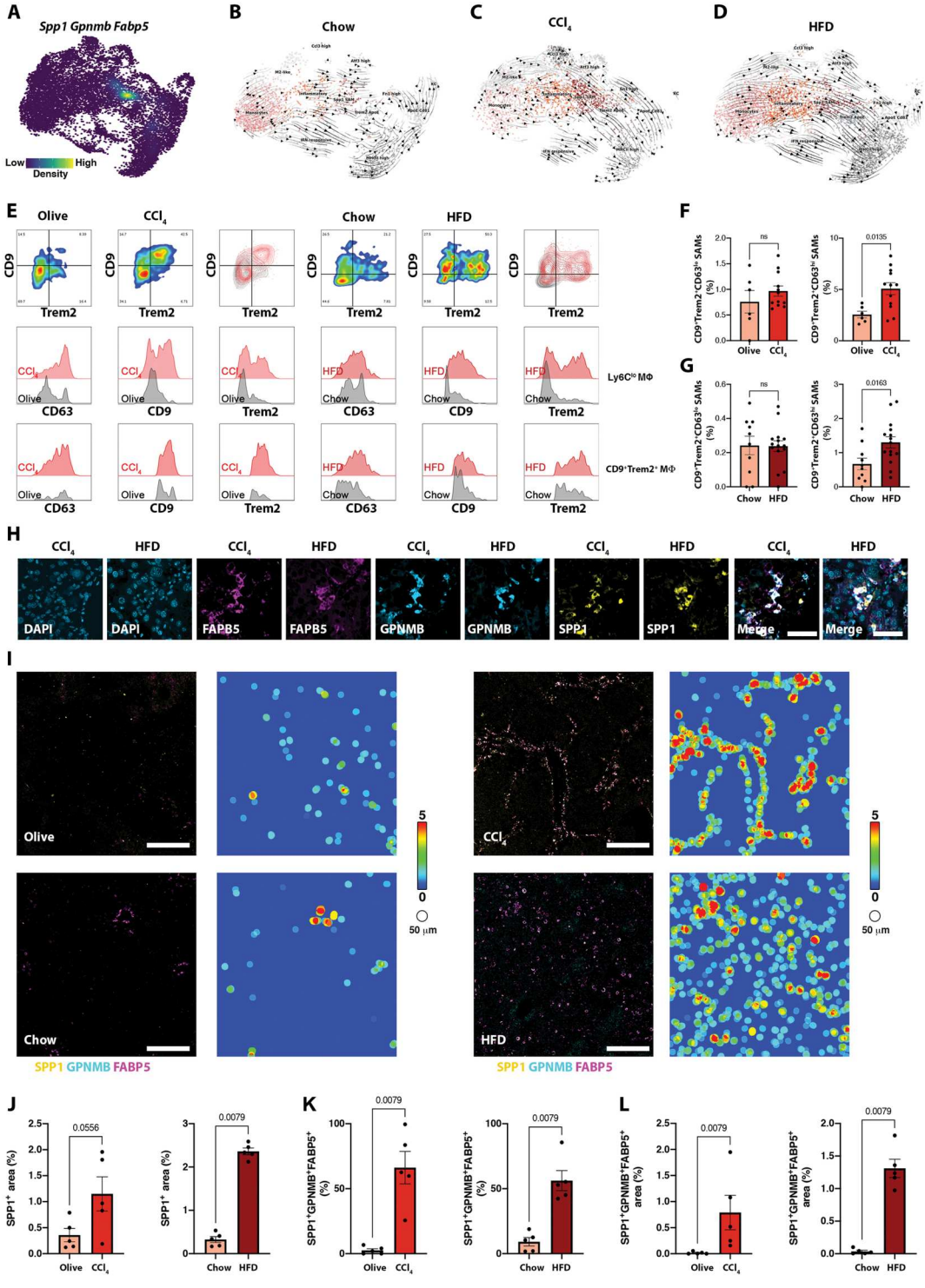

Fig. 4. Fab5 SAMs originate from monocytes based on their transcriptional trajectories and specifically accumulate in fibrotic lesions in two murine liver fibrosis models. (**A**) Nebulosa plot showing joint density of SAM genes *Spp1*, *Gpnmb*, and *Fabp5*. (**B** to **D**) RNA velocity field projected onto UMAP plots of myeloid cells from chow (B), CCl_4 (C), and HFD (D) livers. (**E**) Representative FACS plots of CD9 and Trem2 on $Ly6C^{lo}F4/80^+$ hepatic macrophages from olive (gray), CCl_4 (red), chow (gray), and HFD (dark red). Histograms of CD63, CD9, and Trem2 on $Ly6C^{lo}F4/80^+$ hepatic macrophages and $CD9^+Trem2^+$ SAMs. (**F** and **G**) Frequency of $CD9^+Trem2^+CD63^{lo}$ (left) and $CD9^+Trem2^+CD63^{hi}$ (right) SAMs in CCl_4 (F) and HFD (G). (**H**) High-magnification cycIF staining of SPP1, GPNMB, and FABP5 from CCl_4 and HFD livers. In the merged images on the right, white indicates colocalized expression of all three markers. Scale bars, 25 μm. (**I**) Low-magnification cycIF of SPP1, GPNMB, and FABP5 in olive, CCl_4, chow, and HFD livers and accompanying tissue heatmaps (scale, blue = 0 to red = 5 cells/50 μm) of $SPP1^+$ cells. Scale bars, 500 μm. (**J**) Total SPP1-positive area in CCl_4 (left) and HFD (right) by cycIF. (**K**) Frequency of $SPP1^+GPNMB^+FABP5^+$ SAMs in CCl_4 (left) and HFD (right). (**L**) Area of $SPP1^+GPNMB^+FABP5^+$ SAMs in CCl_4 (left) and HFD (right). Statistics: Mann-Whitney *U* test, *P* values displayed on plots. ns, not significant.

the increase in $CD9^+TREM2^+CD63^{hi}$ macrophages in mouse models of liver fibrosis by flow cytometry (Fig. 4, E to G). Critically, cycIF using the same gating strategy used in patient samples ($SPP1^+GPNMB^+FABP5^+$; Fig. 2, G and H) validated the increase and physical proximity of Fab5 macrophages to the scar (Fig. 4, H and I). This analysis also recapitulated the increased density of SPP1- and triple-positive macrophages seen in human cirrhotic livers (Fig. 4, J to L). Similar analyses performed in the murine bleomycin model of lung fibrosis supported this being a core SAM signature across liver and lung fibrosis (fig. S11).

Downloaded from https://www.science.org at Tsinghua University on October 24, 2025

Type 3 cytokines drive in vitro differentiation of human profibrotic macrophages expressing Fab5 markers

We next explored drivers of the Fab5 signature in vitro using purified human monocytes. We confirmed mixed type 1, 2, and 3 cytokine production by murine intrahepatic lymphocytes from CCl_4 and HFD animals stimulated ex vivo (Fig. 5, A and B). Using cycIF, we confirmed that neutrophils producing type 3 cytokines IL-17A and GM-CSF physically colocalize with macrophages within the hepatic scar in human tissue (Fig. 5C and fig. S12), as was seen in mouse. In addition, we found that TGF-β–activating molecules like integrin β1 (CD29) and matrix metalloproteinase 9 (MMP9) were enriched and colocated in the scar (Fig. 5C and fig. S12). On the basis of the physical proximity between GM-CSF–producing neutrophils and macrophages in the scar, we hypothesized that GM-CSF would drive monocytes toward this signature in vitro. Comparison of M-CSF and GM-CSF differentiation confirmed this hypothesis (Fig. 5, D and E). We then investigated the roles of the main type 1, 2, and 3 cytokines. Type 1 [interferon-γ (IFN-γ)] and 2 (IL-4/IL-13) cytokines inhibited this phenotype, evidenced by fewer $CD9^+TREM2^+$ cells and lower CD63 expression. Conversely, the type 3 cytokines IL-17A and TGF-β1 increased the frequency of macrophages expressing Fab5-associated markers (Fig. 5, F and G).

To determine whether these Fab5-like macrophages were profibrotic, we cocultured them with primary hepatic stellate cells (HSCs) with proinflammatory IFN-γ or profibrotic TGF-β1. As expected, macrophages enhanced TGF-β1–induced collagen type I production by cocultured HSCs, correlating with induction of the Fab5 signature (Fig. 5, H to K). We next investigated whether in vitro differentiated SAMs ($M_{TGF\text{-}\beta}$) showed differential extracellular matrix (ECM)–remodeling activity. GM-CSF–derived macrophages (M0) stimulated with either IFN-γ ($M_{IFN\text{-}\gamma}$) or TGF-β1 ($M_{TGF\text{-}\beta}$) were cultured on DQ-collagen I (scar), DQ-collagen IV, or DQ-gelatin (both "normal" ECM) and fed an MMP-sensitive substrate. $M_{TGF\text{-}\beta}$ demonstrated higher MMP activity when compared with M0 and $M_{IFN\text{-}\gamma}$, which was up-regulated when the macrophages were cultured on normal ECM (Fig. 5, I and L). This phenotype correlated with increased degradation of normal, but not scar, ECM (Fig. 5, J and M). Together, these data indicate that GM-CSF, IL-17A, and TGF-β can collaboratively induce monocyte-to-SAM differentiation and suggest that macrophages expressing markers of Fab5 SAMs degrade normal ECM and promote pathogenic collagen deposition by mesenchymal cells.

Therapeutic TGF-β, IL-17A, or GM-CSF blockade reduced Fab5 macrophages and fibrosis in chronic CCl_4 injury

To validate the in vitro findings implicating TGF-β, IL-17A, and GM-CSF in the differentiation of profibrotic Fab5 SAM, we therapeutically inhibited each of these three cytokines in chronic CCl_4 liver injury. We observed a reduction of fibrosis measured by histology and liver hydroxyproline content in each treatment group (Fig. 6, A and B). As shown previously, fibrosis progression was associated with an increased frequency of myeloid cells by flow cytometry (Fig. 6, C to E). Neutralization of IL-17A or GM-CSF led to a reduced frequency of myeloid cells of $CD45^+$ cells infiltrating the liver, in contrast to TGF-β blockade (Fig. 6, D and E). TGF-β inhibition decreased the frequencies of $Ly6C^{lo}$ macrophages, $CD9^+TREM2^+CD63^{lo}$ macrophages, and $CD9^+TREM2^+CD63^{hi}$ (Fab5) SAMs (Fig. 6, L to O). In contrast, IL-17A or GM-CSF blockade only affected the frequency of Fab5 SAMs (Fig. 6, L to O). Each treatment also reduced the levels of CD63 and GPNMB (Fig. 6, F to K) expressed by these cells, reinforcing our in vitro observation (Fig. 5, L to N). These data validate the importance of TGF-β, IL-17A, and GM-CSF in driving Fab5 SAM differentiation in vivo, suggest that TGF-β works differently from IL-17A and GM-CSF, and further support the connection between Fab5 SAMs and fibrosis severity.

Therapeutic TGF-β blockade reduced murine hepatic and pulmonary Fab5 macrophages and fibrosis

We next investigated whether therapeutic TGF-β inhibition with either a small-molecule inhibitor (ALK5i) or a pan–TGF-β neutralizing antibody (1D11) would reduce Fab5 differentiation in mouse liver and lung fibrosis models. Inhibition of TGF-β led to reduction of liver and lung fibrosis (Fig. 7, A to F). RNA velocity analysis suggested that 1D11 treatment reduced differentiation of monocytes to Fab5 SAM (Fig. 7G). We validated the decrease in Fab5 SAM by flow cytometry (Fig. 7H). There was a decrease in $CD9^+TREM2^+CD63^{lo}$ macrophages in both models of liver fibrosis but no change in the lung (Fig. 7, I, K, and M). There was a decrease in $CD9^+TREM2^+CD63^{hi}$ Fab5 SAMs in the relevant organ for each model, identifying this population as the best correlate with the extent of fibrosis (Fig. 7, J, L, and N). Using cycIF, we demonstrated that whereas there was no decrease in $SPP1^+$ single-positive cells, there was a high reduction in $SPP1^+GPNMB^+FABP5^+$ cell frequency and area with TGF-β inhibition (Fig. 7, O to Q). This result reinforced the earlier finding that a combination of markers is critical for accurate identification of Fab5 SAM across organs and species and demonstrated that TGF-β is important for Fab5 differentiation in both fibrotic tissues.

DISCUSSION

The contributions of macrophages to promoting and resolving fibrosis have been recognized for many years (*10*). Recent work has demonstrated that *CD9*$^+$*TREM2*$^+$ macrophages expand in fibrotic organs (*11*–*13*, *19*); here, we show that the joint expression of these markers is observed in multiple myeloid populations in liver and lung fibrosis. Homeostatic adipose-resident and alveolar macrophages are also *CD9*$^+$*TREM2*$^+$, further supporting the need for additional markers to specifically identify SAMs (*18*). We used our scRNA-seq atlases to determine that combined expression of *SPP1*, *GPNMB*, and *FABP5* or *CD63* was necessary to specifically identify the expanded SAM population among *CD9*$^+$*TREM2*$^+$ myeloid cells. Critically, our defined set of markers can now be used to accurately identify this putatively pathogenic macrophage population.

Given the heterogeneity of macrophages, it was unsurprising that combining multiple markers was required to accurately identify SAMs (*14*). We predict that this level of precision will become standard in defining cell type subpopulations and will harmonize nomenclature. For example, SAMs share marker expression with "lipid-associated macrophages" and "NASH-associated macrophages," among others (*11*, *13*, *21*). However, we and others have demonstrated that SAMs occur regardless of lipid accumulation and in multiple tissues irrespective of NASH status. Thus, we agree with the previous proposal of SAMs as the overarching name for these cells and hypothesize that they will be found in additional fibrotic tissues (*10*). We propose that the definition of a SAM should

Downloaded from https://www.science.org at Tsinghua University on October 24, 2025

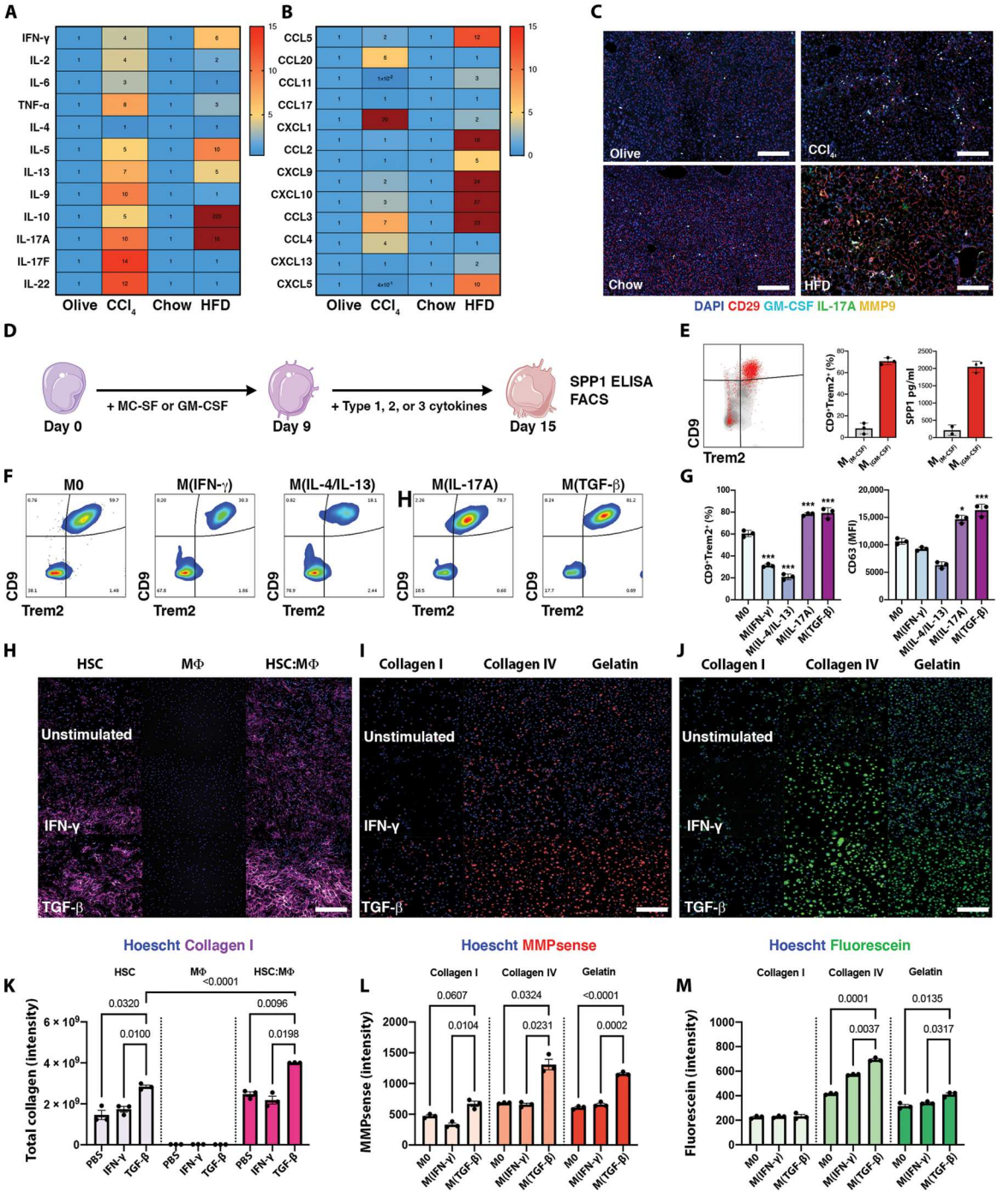

Fig. 5. TGF-β, IL-17A, and GM-CSF are sufficient to induce phenotypic differentiation of SPP1$^+$ SAMs from human monocytes. (**A** and **B**) Heatmap comparing fold change in type 1, 2, and 3 cytokines (A) and chemokines (B) with stimulated intrahepatic lymphocytes from CCl_4, HFD, and respective controls. (**C**) cycIF staining of Iba1, IL-17A, GM-CSF, and MMP9 showing localization of type 3 cytokines in livers. Scale bars, 100 μm. (**D**) Schematic of in vitro macrophage differentiation assay. (**E**) Representative CD9 versus Trem2 FACS plot of M-CSF–derived (gray) or GM-CSF–derived (red) macrophages at day 9. Frequency of CD9$^+$Trem2$^+$ macrophages (left) and SPP1 concentration in supernatant (right) at day 15. (**F**) Representative CD9 versus Trem2 FACS plot of GM-CSF–derived M0, M(IFN-γ), M(IL-4/IL-13), M(IL-17A), and M(TGF-β). (**G**) Frequency of CD9$^+$Trem2$^+$ macrophages after cytokine stimulations (left) and CD63 mean fluorescence intensity (MFI) of GM-CSF–derived M0, M(IFN-γ), M(IL-4/IL-13), M(IL-17A), and M(TGF-β) (right). (**H** and **K**) Representative images of collagen I staining (purple) in mono- or cocultures of macrophages with primary human HSC stimulated with IFN-γ or TGF-β1 (H) and quantification of collagen I average intensity per cell in HSC monoculture (gray), macrophage monoculture (pink), and HSC:macrophage coculture (purple) (K). (**I** and **J**) MMPsense (red, I) or DQ-fluorescein (green, J) staining of macrophages cultured on either DQ-collagen I, DQ-collagen IV, or DQ-gelatin substrates stimulated with either IFN-γ or TGF-β1. Scale bars, 250 μm (H and J). (**L** and **M**) Quantification of MMPsense per cell (L) and fluorescein per well (M) from macrophages cultured on either DQ-collagen I (light color), DQ-collagen IV (color), or DQ-gelatin (dark color) substrates stimulated with either IFN-γ or TGF-β1. Statistics: ANOVA or two-way ANOVA followed by a post hoc Tukey, *P* values displayed on plots. ELISA, enzyme-linked immunosorbent assay.

Downloaded from https://www.science.org at Tsinghua University on October 24, 2025

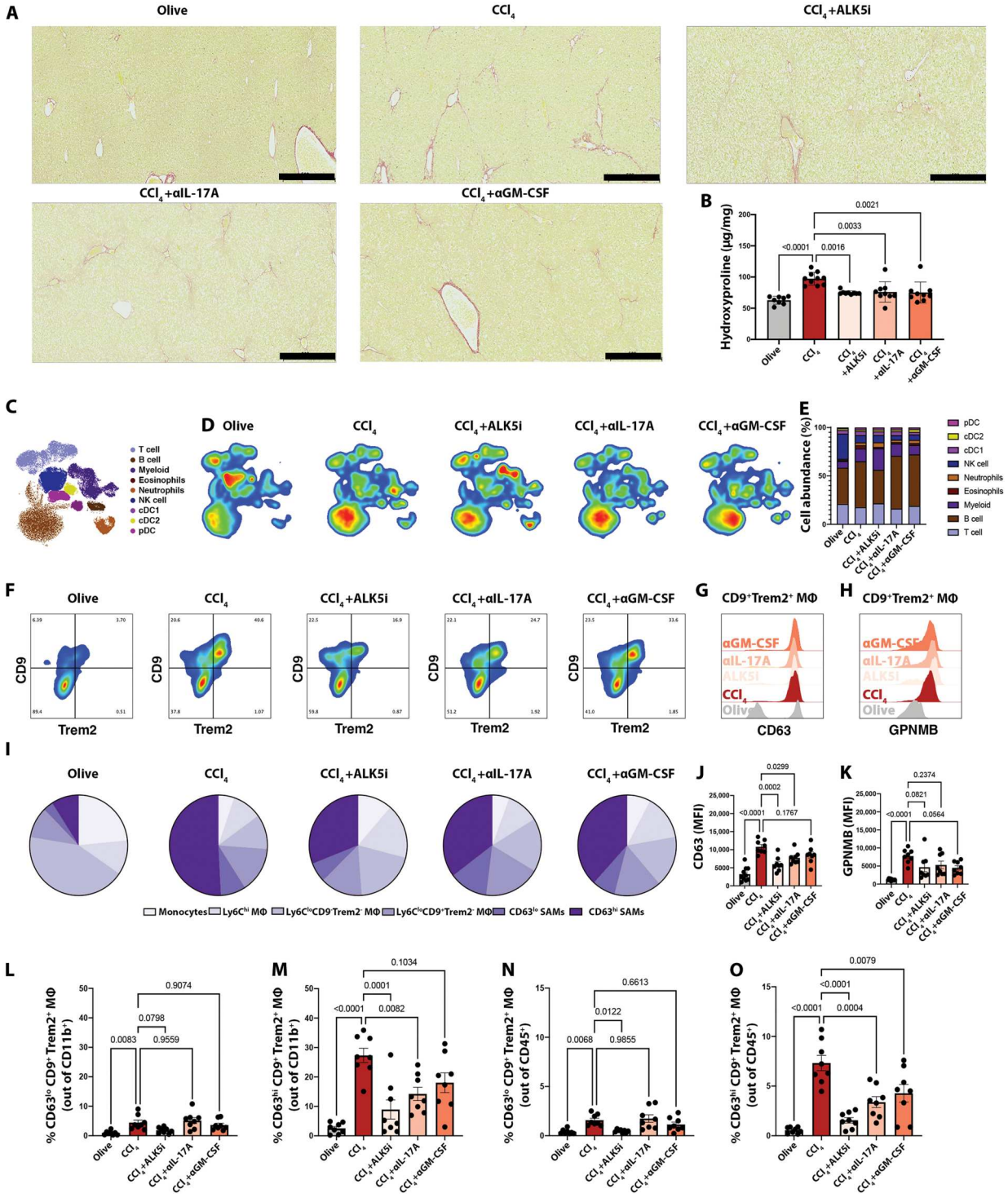

Fig. 6. Therapeutic TGF-β, IL-17A, or GM-CSF blockade inhibits the differentiation of CD63$^+$SPP1$^+$ SAMs and liver fibrosis. (**A**) Representative picro Sirius red staining of olive oil–, CCl_4-, CCl_4 + ALK5i–, CCl_4 + anti–IL-17A–, and CCl_4 + anti–GM-CSF–treated livers. Mice from these groups were analyzed for all subsequent panels in this figure. (**B**) Quantification of liver hydroxyproline content. (**C**) UMAP FACS plot of liver leukocytes colored by cell type. (**D**) UMAP FACS density plots of liver leukocytes per treatment group. (**E**) Stacked bar chart of liver leukocyte populations as a percentage of hepatic CD45$^+$ cells per treatment group. (**F**) Representative FACS plots of CD9 and Trem2 on Ly6C^{lo}F4/80$^+$ liver macrophages per treatment group. (**G** and **H**) Histograms of CD63 (G) and GPNMB (H) expression on CD9$^+$Trem2$^+$ liver macrophages per treatment group. (**I**) Pie charts representing the frequencies of monocytes, Ly6C^{hi} macrophages, CD9^{neg}Trem2^{neg} macrophages, CD9$^+$Trem2^{neg} macrophages, CD63^{lo} SAMs, and CD63^{hi} macrophages of hepatic CD11b$^+$ cells per treatment group. (**J** and **K**) Quantification of CD63 (J) and GPNMB (K) MFI on CD9$^+$Trem2$^+$ liver macrophages per treatment group. (**L** and **M**) Frequencies of liver CD9$^+$Trem2$^+$CD63^{lo} (L) and CD9$^+$Trem2$^+$CD63^{hi} (M) SAMs of CD11b$^+$ cells. (**N** and **O**) Frequencies of liver CD9$^+$Trem2$^+$CD63^{lo} (N) and CD9$^+$Trem2$^+$CD63^{hi} (O) SAMs of CD45$^+$ cells. Statistics: ANOVA or two-way ANOVA followed by a post hoc Tukey, *P* values displayed on plots. Scale bars, 250 μm.

Downloaded from https://www.science.org at Tsinghua University on October 24, 2025

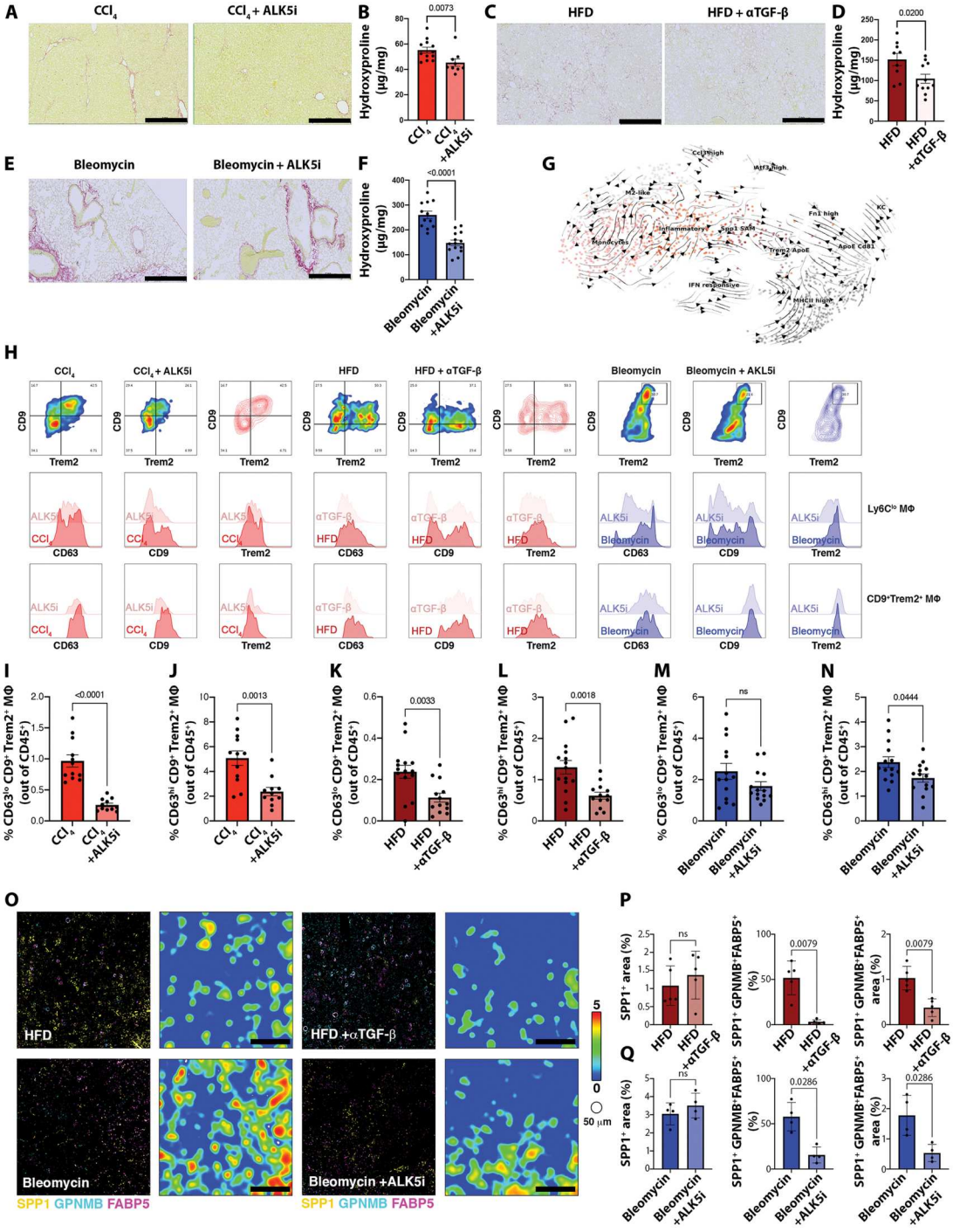

Fig. 7. Therapeutic TGF-β blockade inhibits differentiation of SPP1$^+$ SAMs and fibrosis in murine models of liver and lung disease. (**A**) Representative picro Sirius red staining of CCl_4- and CCl_4 + ALK5i–treated livers. (**B**) Quantification of liver hydroxyproline content in CCl_4 injury. (**C**) Representative picro Sirius red staining of HFD- and HFD + anti–TGF-β–treated livers. (**D**) Quantification of liver hydroxyproline content in HFD. (**E**) Representative picro Sirius red staining of bleomycin- and bleomycin + ALK5i–treated lungs. (**F**) Quantification of lung hydroxyproline content in bleomycin injury. (**G**) RNA velocity field projected onto a UMAP plot of liver myeloid cells from HFD mice treated with anti–TGF-β blocking antibody. (**H**) Representative FACS plots of CD9 and Trem2 on Ly6C^{lo}F4/80$^+$ macrophages and histograms of CD63, CD9, and Trem2 on Ly6C^{lo}F4/80$^+$ macrophages and CD9$^+$Trem2$^+$ SAMs in CCl_4 (red), CCl_4 + ALK5i (salmon), HFD (dark red), HFD + anti–TGF-β (bordeaux), bleomycin (blue), and bleomycin + ALK5i (light blue) by FACS. (**I** to **N**) Frequencies of CD9$^+$Trem2$^+$CD63^{lo} (I, K, and M) and CD9$^+$Trem2$^+$CD63^{hi} (J, L, and N) SAMs in CCl_4 (red) and CCl_4 + ALK5i (salmon) (I and J), HFD (dark red) and HFD + anti–TGF-β (bordeaux) (K and L), and bleomycin (blue) and bleomycin + ALK5i (light blue) (M and N) by FACS. (**O**) cycIF staining of SPP1, GPNMB, and FABP5 from HFD and HFD + anti–TGF-β (top) or bleomycin and bleomycin + ALK5i (bottom). Representative tissue heatmaps (scale, blue = 0 to red = 5 cells per 50 μm) of SPP1$^+$ cells. (**P** and **Q**) Total SPP1$^+$ area (left), frequency of SPP1$^+$GPNMB$^+$FABP5$^+$ SAMs (middle), and area of SPP1$^+$GPNMB$^+$FABP5$^+$ SAMs (right) in HFD and HFD + anti–TGF-β (P) or bleomycin and bleomycin + ALK5i (Q). Statistics: ANOVA or two-way ANOVA followed by a post hoc Tukey, *P* values displayed on plots. Scale bars, 500 μm.

Downloaded from https://www.science.org at Tsinghua University on October 24, 2025

include: (i) expansion in a fibrotic tissue; (ii) physical proximity to excessive ECM; and (iii) expression of at least five markers among TREM2, CD9, SPP1, GPNMB, FABP5, and CD63. If direct, formal proof of a function can be consistently ascribed to SAMs across fibrotic tissues, this should be included in the definition. This can be difficult: Selective in vivo depletion of a subpopulation defined by multiple markers is logistically challenging, and direct ex vivo studies of a relatively rare cell population sorted from tissues come with challenges and caveats. At this time, such proof is elusive, with conclusions based on correlative or weight-of-evidence results, as was done here.

"Scar-associated" does not imply profibrotic. Several studies indicate that TREM2, which Fab5 SAMs express, protects against fibrosis. This is likely because of increased inflammation and cell death, and decreased clearance of lipids and cellular debris, in *Trem2* knockout animals. However, interpretation of *Trem2* knockouts is complicated by its expression by many myeloid cells and, perhaps most importantly, its role in myelopoiesis (Fig. 2 and fig. S10) (*19*, *28*–*31*). Deleting *Trem2*, globally or in a tissue- or cell-type manner, would therefore not be expected to phenocopy "Fab5 depletion." Despite expressing some proteins with antifibrotic functions, like TREM2, we hypothesize that the sum of Fab5 SAM functions is profibrotic. To this point, we showed that macrophages differentiated to adopt Fab5 markers in vitro enhance deposition of collagen I by HSCs and had increased MMP activity that correlated with enhanced degradation of normal ECM substrates. This is consistent with conditioned medium from primary human $CD9^+$ $TREM2^+$ cirrhosis-associated macrophages inducing fibrillar collagen gene expression by HSC (*11*). In addition, Fab5 SAMs express a variety of genes associated with fibrosis progression: CD63 contributes to integrin β1/3–mediated activation of TGF-β and enhances SMAD3 signaling through the β-catenin pathway (*32*); GPNMB contributes to the degradation and recycling of collagen IV, a normal constituent of liver ECM, and is genetically associated with driving fibrosis progression (*33*, *34*); SPP1 and FABP5 positively modulate T helper 17 (T_H17) responses to potentially fuel a feed-forward loop, leading to increased IL-17A, GM-CSF, and TGF-β (*35*, *36*).

Whereas we observed mixed inflammatory signals in our preclinical models of fibrosis, as in human diseases, scars were enriched in IL-17A–, GM-CSF–, and TGF-β–activating MMP9 and CD29 (*8*, *9*, *37*). This led us to hypothesize that type 3 cytokines drive SAM differentiation. We provide evidence that infiltrating monocytes in liver and lung fibrosis differentiate into Fab5 SAMs in response to IL-17A, GM-CSF, and TGF-β, consistent with previous genetic fate-tracing and computational approaches (*11*, *12*, *20*, *21*). In vitro, we showed that these factors drove human monocytes to express Fab5 markers. Consistent with our in vitro data, we observed a decrease in Fab5 SAMs upon in vivo blockade of each cytokine (Fig. 6), which correlated with decreased fibrosis in murine models. Although our data support that type 3 inflammation and TGF-β are required for differentiation of Fab5 SAMs, further studies should characterize the phenotype and function of SAMs in type 2 cytokine–driven fibrosis.

Our lack of direct in vivo evidence of a fibrogenic role for Fab5 SAMs is one of the limitations of this study. The use of genetic models with time- and cell-specific depletion of Fab5 SAMs or fibrogenic effectors in future studies will address this shortcoming. Another limitation is that we provide only indirect evidence of infiltrating monocytes being the major precursor for Fab5 SAMs. As demonstrated by others, future studies could address this by using inducible fate-tracing systems and parabiosis experiments (*12*, *14*, *15*, *20*, *26*). In addition, we did not study fibrosis caused by infectious diseases, which can have different inflammatory skewing than sterile injury–driven fibrosis. This can be addressed by complementing sterile injury models with *Schistosoma mansoni* or chronic viral infection and other fibrosis models of infectious origin.

In conclusion, we used an unbiased approach to expand on the previous identification of SAMs and provide a unifying set of markers across species, organs (liver and lung), and techniques. We propose that Fab5 SAMs, arising from monocytes and differentiated by IL-17A and GM-CSF produced by neutrophils and active TGF-β1 in the niche, promote the deposition of pathogenic ECM by contributing to the activation of mesenchymal cells and clearing normal ECM. We have accomplished this using a workflow starting from human scRNA-seq datasets, followed by validation of populations of interest in animal models, to prioritize strategies and targets for future validation. Although we have used this approach to identify a well-defined population of SAMs that represent a promising target population for the treatment of human fibrotic diseases, a generalized version of this workflow could be applied to other human diseases to aid in the development of a wide range of therapies.

MATERIALS AND METHODS

Study design

This study was designed to identify macrophage subsets that expand during fibrosis and to determine whether these subsets are common across tissues, species, and etiologies of fibrosis. An additional goal was to define factors contributing to the differentiation or activation of these macrophage subsets. We accomplished this using patient samples that were either previously published or collected under regulatory approval and with consent at multiple sites and murine models of lung and liver fibrosis. Using scRNA-seq, flow cytometry, and advanced in situ imaging, we identified a macrophage subset that expands in liver and lung fibrosis and is associated with scarring across species and derived precise five-marker (Fab5) signatures to identify these cells by multiple methods. By combining in vitro primary human cell culture assays with in vivo antagonism, we demonstrated that GM-CSF, TGF-β1, and IL-17A drive the differentiation of FAB5 macrophages, which augment the fibrogenic activation of mesenchymal cells. Tissue sections for imaging and samples for flow cytometry and hydroxyproline measurements were blinded before processing and quantification by multiple independent researchers and were unblinded for statistical analysis and graphing. The samples we used for scRNA-seq were unblinded throughout quantification and analysis. Our descriptions of independent technical and biological replicates are included in the figure legends and tables (data file S1). When technical or processing errors were recorded, we excluded data from those samples from our final quantification and statistical analyses.

Mouse strains and models

All experimental procedures were performed at Pfizer (Cambridge, MA) and approved by the Institutional Animal Care and Use Committee. C57BL/6 male mice ($N = 8$ per group), 8 to 10 weeks of age

Downloaded from https://www.science.org at Tsinghua University on October 24, 2025

(the Jackson Laboratory, Bar Harbor, ME), were used for the CCl_4 and bleomycin models. The mice were maintained in a controlled environment with a temperature of 70° to 72°F, humidity of 30 to 70%, and a photo cycle of 12 hours of light and 12 hours of dark. They were provided with PicoLab rodent diet 20 (5053, Purina Mills Inc., Lab Diet, St. Louis, MO, unless otherwise indicated for HFDs) and standard drinking water ad libitum. For CCl_4 liver injury, mice were dosed 2 ml/kg intraperitoneally twice weekly with either olive oil ($N = 8$) or CCl_4 [CCl_4:olive oil, 1:3 (v/v), Sigma-Aldrich, St. Louis, MO] for 4 weeks. Mice in CCl_4 studies were euthanized with CO_2 at study end. For bleomycin lung injury, on day 0, animals were intratracheally challenged with 75 mg of bleomycin (EMD Millipore, Burlington, MA) in a volume of 25 ml. Seven days later, mice were therapeutically dosed with vehicle, ALK5 inhibitor (SB-525334), for a duration of 14 days. At termination of bleomycin lung injury studies, mice were anesthetized with isoflurane, exsanguinated, and euthanized via cervical dislocation. For preclinical NASH studies, C57BL/6 male mice, 6 to 8 weeks of age (the Jackson Laboratory, Bar Harbor, ME), were fed either control (D09100304) or high-fat (D09100310) diet (Research Diets, New Brunswick, NJ) for 34 weeks to induce disease phenotype. Shear wave elastography was performed before therapeutic treatment, and animals were randomized into treatment groups on the basis of average liver stiffness. After randomization, animals were singly housed except for control animals, which were group-housed. Animals in the control group ($N = 8$) were maintained on control chow through week 44. HFD treatment groups included immunoglobulin G1 (IgG1) isotype control ($N = 13$, 10 mg/kg; PF-00713222-0010) and TGF-β antibody 1D11 ($N = 13$, 10 mg/kg; BP0057 lot no. 704719 J1, Bio X Cell, West Lebanon, NH).

Human tissue sections

The study was approved by the National Health Service national research ethics service under approval numbers 16/NE/0230 and 11/NE/0291. It used nondiseased human donor lungs that were not used in clinical transplantation and when consent from the donor next of kin was given for organ research. Explant IPF lung tissue was collected from patients undergoing either double or single lung transplantations at the Freeman Hospital, Newcastle upon Tyne.

Anonymized, formalin-fixed paraffin-embedded (FFPE) liver tissue was acquired from BioIVT under written informed consent. Patient information can be found in table S1.

Human scRNA-seq preprocessing and analysis

Gene expression matrices [GSE136103 (*11*), HCA project SingleCellLiverLandscape (*38*), GSE185477 (*39*), GSE125188 (*40*), GSE156625 (*41*), GSE192740 (*42*), GSE122960 (*16*), GSE128033 (*18*), GSE128169 (*43*), GSE135893 (*44*), and GSE132771 (*45*)] were processed using Seurat (v4.0.3). Ribosomal genes were removed, and gene symbols were unified using the biomaRt package (*46*). Cells were filtered using cutoffs of minimum 500 genes per cell and maximum 20% mitochondrial reads. Samples were limited to 10x Chemistry v2 or v3. Genes per cell, transcript counts per cell, and mitochondrial read percentage per cell are presented in figs. S1 to S3 (for the human liver, lung, and myeloid atlases, respectively). Lung myeloid cells were limited to donors containing greater than 300 cells and downsampled to match the number of liver myeloid cells.

Seurat was used for dimensionality reduction, cell clustering, and differential gene analysis. Human single-cell objects were split by dataset and chemistry and normalized using SCTransform with percent mitochondrial reads regressed out (*47*). After one round of clustering, nonmyeloid doublet cells were removed. The top 750 variable features from each liver dataset and 1000 variable features from each lung dataset were combined and used in downstream steps. Harmony (*48*) was used to correct for patient, dataset, and chemistry variability, and 40 principal components (PCs) were used for RunUMAP and FindNeighbors. A resolution of 0.6 was used for cluster selection. FindAllMarkers was used to identify markers for clusters, and annotation was performed manually using the markers shown in figs. S1 to S3 (for the human liver, lung, and myeloid atlases, respectively).

Tissue processing

Murine liver and lung were collected in RPMI 1640 medium on ice, minced, and digested in collagenase (100 U/ml; Sigma-Aldrich) at 37°C for 1 hour with shaking. Digested tissue was filtered through 70-μm nylon mesh, and hepatocytes were removed by spinning at 50*g* for 3 min. The remaining cells were passed through a 25% Percoll (GE Life Sciences) gradient, and erythrocytes were lysed with ammonium-chloride-potassium buffer. Single cells were aliquoted for flow cytometry or pooled and distributed for restimulation and scRNA-seq.

Multiplex cytokine analysis

Intrahepatic leukocytes or intrapulmonary leukocytes were resuspended at a concentration of 5 million cells per ml in RPMI with 10% fetal bovine serum (FBS) and 1× stimulation cocktail (eBioscience) for 18 hours. Supernatants were collected and frozen before cytokine quantification. Multiplex cytokine or chemokine quantification was performed on 25 ml of supernatant using LEGENDplex (BioLegend). Analysis was performed using BioLegend analysis software. Data were normalized to naïve animals and expressed as fold change.

Flow cytometry

Murine and human cells were washed with phosphate-buffered saline (PBS) and stained with LIVE/DEAD fixable aqua viability dye (Invitrogen). After washing with fluorescence-activated cell sorting (FACS) buffer, cells were fixed with Foxp3/Transcription Factor Fixation/Permeabilization buffer (Invitrogen). After washing, cells were resuspended in 90% FACS buffer/10% dimethyl sulfoxide (DMSO) and stored at −80°C until antibody staining and flow cytometry were performed.

After thawing, cells were washed, and Fc receptors were blocked with TruStain FcX (mouse or human, as appropriate; BioLegend) before staining with diluted antibodies (table S2). Cells were then washed, filtered through 60-μm mesh, and run on an LSRFortessa (BD). Data were analyzed in FlowJo version 10.5+ (BD) using the DownSample and UMAP (Uniform Manifold Approximation and Projection) plugins. Example gating strategies are depicted in figs. S13 and S14.

cycIF staining and analysis

cycIF was performed as described by Molina *et al.* (*49*) using the antibodies described in tables S2 and S3. Briefly, FFPE sections of human or murine liver or lung specimens were deparaffinized,

Downloaded from https://www.science.org at Tsinghua University on October 24, 2025

rehydrated, and subjected to heat-induced epitope retrieval. After blocking with normal donkey serum, slides were stained with primary antibodies overnight (table S4). Unbound antibodies were removed by washing, and slides were stained with fluorescently conjugated secondary antibodies made in donkeys (table S5). Slides were again washed, DNA-stained with 4′,6-diamidino-2-phenylindole (DAPI; Invitrogen), and mounted in ProLong Diamond Antifade Mountant with DAPI (Invitrogen). Stained slides were imaged using Axioscan (Zeiss). After each round of imaging, coverslips were removed and antibodies were stripped.

Acquired images were first subjected to shading correction and stitching using the Zeiss ZEN blue DESK (version 3.0) image processing software. The alignment across subsequent rounds was performed on their respective nuclear (DAPI) channel via FIJI and applying the transformation to the remaining channels (*50*, *51*). The multichannel image pyramid was generated using Bioformats2-Raw and Raw2OMETiff programs (both Glencoe Software, Seattle, WA) and lastly loaded into Visiopharm (Visiopharm A/S, Denmark) for analyses. A representative 2 mm × 2 mm region of interest was centered on the tissue, where segmentation and heatmap applications (APPs) were applied for individual markers. All APPs were run with the same parameters across the experimental groups within the same tissue type to ensure data integrity. Numerical values were extracted and processed using Microsoft Excel and R and converted to a FlowJo-compatible format (FCS) for further analyses.

Histology

FFPE sections were deparaffinized before incubation in Picro Sirius Red solution (Direct Red 81 0.2% in 1.3% picric acid solution, Sigma-Aldrich). Sections were rinsed in dH_2O, dried, mounted with Permount (Thermo Fisher Scientific), and acquired on a Leica system. Red pixels were quantified as percent area of fibrosis.

Murine scRNA-seq and data analyses

Cells isolated from murine livers were stained with Hoechst 33342 (30 μg/ml; Miltenyi) and Zombie NIR viability dye (diluted 1:250 in PBS; BioLegend) before FACS sorting (Sony SH800) to obtain live, single cells. These were methanol-fixed on the basis of the 10x Genomics recommended fixation protocol and stored at −80°C before encapsulation and barcoding on a Chromium Controller (10x Genomics, Pleasanton, CA). The 3′ sequencing library construction followed the protocols for 10x Genomics Single Cell version 2 or version 3.1. Samples from some experiments were lipid-hashed as described by McGinnis *et al.* before encapsulation except using commercially available 5′ or 3′ cholesterol–triethylene glycol (TEG)–tagged oligos as the anchor and coanchor. For these samples, sequencing libraries were constructed as described previously (*52*). Libraries were sequenced on Illumina NextSeq 500/550.

Expression FASTQs were preprocessed with Cell Ranger (10x Genomics) using the default settings and aligned to the provided mm10 reference genome [Ensembl 93, 10x Genomics, (*53*)]. These were further preprocessed through the velocyto package using the run10x wrapper, mm10 genome above, and mm10 repeat mask [UCSC Genome Browser, https://genome.ucsc.edu/index.html, (*54*, *55*)] Count matrices for gene expression, hashing barcodes, and spliced, unspliced, and ambiguous reads were combined into a single Seurat object for each sample or sequencing lane [Seurat version 4.0.3 (*56*), R version 4.0.0, RStudio version 1.2.5042]. Lipid-hashed samples were demultiplexed as described by McGinnis *et al.* (*52*) or using HTODemux in Seurat (*56*, *57*). Aligned, demultiplexed matrices from all experiments were combined, and barcodes with greater than 25% mitochondrial reads and obvious multiplets (clusters identified by known marker genes of at least two cell types) were removed. Genes per cell, transcript counts per cell, and mitochondrial read percentage per cell are presented in fig. S6.

Seurat was used for dimensionality reduction, cell clustering, and differential gene analysis as described above with the following changes. Murine single-cell objects were split by experiment and normalized as above. The top 3000 variable features were combined and used in downstream steps. Integration was performed across experiments using Harmony (*48*). Sixteen PCs were used for RunUMAP and FindNeighbors, and cluster selection was performed using a resolution of 0.1 based on ClusTree stability diagrams (*58*). Clusters were manually annotated using the markers shown in fig. S4. For high-resolution analysis of monocyte and macrophage populations, this subset was extracted, renormalized, and reintegrated as above using 3000 variable features. Twenty PCs were used for RunUMAP and FindNeighbors. Cluster markers were identified with FindAllMarkers, and clusters were manually annotated by comparing cluster marker lists with prior publications and the human dataset presented here [(*5*, *12*, *14*, *17*–*19*, *21*, *26*) and fig. S6].

RNA velocity was modeled using the scVelo package (*55*, *59*). Briefly, the myeloid compartment counts were normalized, and cells were clustered and annotated as previously described using Seurat. The cells were separated into their respective treatment groups, and velocity was calculated using the functions tl.recover_dynamics and tl.velocity from the scVelo package (default settings and mode = "dynamical").

Hydroxyproline quantification

Liver and lung hydroxyproline content was quantified as previously described (*9*). Tissues (100 to 200 mg) were hydrolyzed in 1 ml of 6 N HCl at 110°C overnight. Ten microliters of the hydrolyzed sample or standard were placed in 30 μl of citric acetate buffer [10 g of citric acid (5%, w/v), 2.4 ml of glacial acetic acid (1.2%, v/v), 14.48 g of sodium acetate (7.24%, w/v), and 6.8 g of sodium hydroxide (3.4%, w/v) with a total volume of 200 ml made up with sterile deionized water]. One hundred microliters of chloramine T solution (0.282 g of chloramine T, 2 ml of isopropanol, 2 ml of sterile water, and 16 ml of citrate acetate buffer) were mixed with the samples or standards and oxidized for 20 min at room temperature. Oxidized samples or standards received 100 μl of Ehrlich′s reagent (2.5 g of *p*-dimethylaminobenzaldehyde, 9.3 ml of isopropanol, and 3.9 ml of 70% perchloric acid) and incubated at 65°C for 20 min. Optical density at 550 nm was recorded and compared with the standard curve for quantification.

In vitro macrophage differentiation

Cryopreserved primary human $CD14^+$ monocytes (STEMCELL Technologies) isolated from peripheral blood were plated at 300,000 cells per well in flat bottom, tissue culture–treated 96-well plates (BD Falcon) in RPMI 1640 supplemented with 10% FBS, 10 mM Hepes, and 2 mM GlutaMax (all Gibco). Monocytes were cultured in recombinant human GM-CSF or M-CSF (10 ng/ml; both BioLegend) for 7 days at 37°C, 5% CO_2 in normoxic

Downloaded from https://www.science.org at Tsinghua University on October 24, 2025

conditions. Media and cytokines were refreshed on day 3 of culture. The conditioned medium was frozen at −80°C. Macrophages were washed with PBS and detached by incubating in cold PBS at 4°C for at least 30 min followed by vigorous pipetting and scraping.

In vitro macrophage/stellate coculture

Primary human $CD14^+$ monocytes were isolated from leukopaks (Research Blood Components) using RosetteSep negative selection (STEMCELL Technologies) over Ficoll gradients (GE Healthcare). Purified monocytes were cultured in RPMI 1640 with 10% FBS, penicillin-streptomycin, and recombinant human GM-CSF (20 ng/ml) in Teflon bags at 37°C, 5% CO_2, and normoxia for 9 days. Differentiating monocytes were fed on days 3 and 7. Differentiated monocyte-derived macrophages (MDMs) were harvested and frozen in 90% FBS/10% DMSO and stored in liquid nitrogen.

Allogeneic primary human HSCs (used between passages 4 and 8) and primary human GM-CSF MDMs were cultured in collagen I–coated CellCarrier Ultra 96-well black walled plates (PerkinElmer) at a ratio of 1425 HSC:28,500 MDM in Fibroblast Growth Basal Medium (FBM) (Lonza) supplemented with 0.2% FBS (Gibco) and 300 mM L-ascorbic acid 2-phosphate (Sigma-Aldrich). Recombinant human IFN-γ (BioLegend) and recombinant human TGF-β1 (BioLegend) were used at final concentrations of 10 ng/ml. Cocultures were incubated for 7 days at 37°C, 5% CO_2 in normoxic conditions without changing the media or refreshing cytokines. Cells were fixed with cold 95% methanol/5% glacial acetic acid (Sigma-Aldrich) and washed extensively with PBS. Blocking was performed with 5% normal goat serum (Gibco) followed by staining with mouse IgG2a anti-human α-smooth muscle actin (clone 1A4, Sigma-Aldrich) and mouse IgG1 anti–collagen I (clone Col1, Sigma-Aldrich). Primary antibodies were detected with goat anti-mouse IgG2a Alexa Fluor 647 and goat anti-mouse IgG1 Alexa Fluor 568 (both Invitrogen). Cytoplasm was detected with HCS CellMask Green (Invitrogen), and nuclei were detected with Hoechst 33342 (BD Biosciences). Imaging was performed on an Opera Phenix (PerkinElmer) with a 10× objective. Total collagen I intensity is presented without normalizing to cell number because macrophages plated alone did not produce detectable collagen I.

Statistical analysis

All statistical tests were conducted using R version 4.0.0 (https://r-project.org/) or Prism version 9. Differential expression testing was performed in R using Seurat version 4.0.0. Graphs were generated using GraphPad Prism 9 (GraphPad Software, La Jolla, CA), the R (version 4.0.0) packages Seurat version 4.0.0 (*56*), ggplot2 version 3.3.5, and Nebulosa version 0.99.92 (*60*) in RStudio (version 1.2.5042), Visiopharm, or FlowJo. Differences between two groups were determined by Mann-Whitney test, whereas differences between groups were determined by analysis of variance (ANOVA) followed by Tukey post hoc test. Kruskal-Wallis test was used when group sizes were too different and if the data did not meet the assumption of homogeneity of variance.

Supplementary Materials

This PDF file includes:
Figs. S1 to S14
Tables S1 to S5

Other Supplementary Material for this manuscript includes the following:
Data file S1
MDAR Reproducibility Checklist

View/request a protocol for this paper from *Bio-protocol*.

REFERENCES AND NOTES

1. R. L. Gieseck III, M. S. Wilson, T. A. Wynn, Type 2 immunity in tissue repair and fibrosis. *Nat. Rev. Immunol.* **18**, 62–76 (2017).
2. N. C. Henderson, F. Rieder, T. A. Wynn, Fibrosis: From mechanisms to medicines. *Nature* **587**, 555–566 (2020).
3. T. Tsuchida, S. L. Friedman, Mechanisms of hepatic stellate cell activation. *Nat. Rev. Gastroenterol. Hepatol.* **14**, 397–411 (2017).
4. V. Cottin, N. A. Hirani, D. L. Hotchkin, A. M. Nambiar, T. Ogura, M. Otaola, D. Skowasch, J. S. Park, H. K. Poonyagariyagorn, W. Wuyts, A. U. Wells, Presentation, diagnosis and clinical course of the spectrum of progressive-fibrosing interstitial lung diseases. *Eur. Respir. Rev.* **27**, 180076 (2018).
5. S. A. Eming, T. A. Wynn, P. Martin, Inflammation and metabolism in tissue repair and regeneration. *Science* **356**, 1026–1030 (2017).
6. P. Bedossa, Pathology of non-alcoholic fatty liver disease. *Liver Int.* **37**(suppl. 1), 85–89 (2017).
7. T. A. Wynn, K. M. Vannella, Macrophages in tissue repair, regeneration, and fibrosis. *Immunity* **44**, 450–462 (2016).
8. K. M. Hart, T. Fabre, J. C. Sciurba, R. L. Gieseck III, L. A. Borthwick, K. M. Vannella, T. H. Acciani, R. de Queiroz Prado, R. W. Thompson, S. White, G. Soucy, M. Bilodeau, T. R. Ramalingam, J. R. Arron, N. H. Shoukry, T. A. Wynn, Type-2 immunity is protective in metabolic disease but exacerbates NAFLD collaboratively with TGF-β. *Sci. Transl. Med.* **9**, eaal3694 (2017).
9. T. Fabre, M. F. Molina, G. Soucy, J. P. Goulet, B. Willems, J. P. Villeneuve, M. Bilodeau, N. H. Shoukry, Type 3 cytokines IL-17A and IL-22 drive TGF-β–dependent liver fibrosis. *Sci. Immunol.* **3**, eaar7754 (2018).
10. J. S. Duffield, S. J. Forbes, C. M. Constandinou, S. Clay, M. Partolina, S. Vuthoori, S. Wu, R. Lang, J. P. Iredale, Selective depletion of macrophages reveals distinct, opposing roles during liver injury and repair. *J. Clin. Invest.* **115**, 56–65 (2005).
11. P. Ramachandran, R. Dobie, J. R. Wilson-Kanamori, E. F. Dora, B. E. P. Henderson, N. T. Luu, J. R. Portman, K. P. Matchett, M. Brice, J. A. Marwick, R. S. Taylor, M. Efremova, R. Vento-Tormo, N. O. Carragher, T. J. Kendall, J. A. Fallowfield, E. M. Harrison, D. J. Mole, S. J. Wigmore, P. N. Newsome, C. J. Weston, J. P. Iredale, F. Tacke, J. W. Pollard, C. P. Ponting, J. C. Marioni, S. A. Teichmann, N. C. Henderson, Resolving the fibrotic niche of human liver cirrhosis at single-cell level. *Nature* **575**, 512–518 (2019).
12. J. S. Seidman, T. D. Troutman, M. Sakai, A. Gola, N. J. Spann, H. Bennett, C. M. Bruni, Z. Ouyang, R. Z. Li, X. Sun, B. T. Vu, M. P. Pasillas, K. M. Ego, D. Gosselin, V. M. Link, L. W. Chong, R. M. Evans, B. M. Thompson, J. G. McDonald, M. Hosseini, J. L. Witztum, R. N. Germain, C. K. Glass, Niche-specific reprogramming of epigenetic landscapes drives myeloid cell diversity in nonalcoholic steatohepatitis. *Immunity* **52**, 1057–1074.e7 (2020).
13. X. Xiong, H. Kuang, S. Ansari, T. Liu, J. Gong, S. Wang, X. Y. Zhao, Y. Ji, C. Li, L. Guo, L. Zhou, Z. Chen, P. Leon-Mimila, M. T. Chung, K. Kurabayashi, J. Opp, F. Campos-Perez, H. Villamil-Ramirez, S. Canizales-Quinteros, R. Lyons, C. N. Lumeng, B. Zhou, L. Qi, A. Huertas-Vazquez, A. J. Lusis, X. Z. S. Xu, S. Li, Y. Yu, J. Z. Li, J. D. Lin, Landscape of intercellular crosstalk in healthy and NASH liver revealed by single-cell secretome gene analysis. *Mol. Cell* **75**, 644–660.e5 (2019).
14. A. Remmerie, L. Martens, T. Thoné, A. Castoldi, R. Seurinck, B. Pavie, J. Roels, B. Vanneste, S. De Prijck, M. Vanhockerhout, M. B. A. Latib, L. Devisscher, A. Hoorens, J. Bonnardel, N. Vandamme, A. Kremer, P. Borghgraef, H. Van Vlierberghe, S. Lippens, E. Pearce, Y. Saeys, C. L. Scott, Osteopontin expression identifies a subset of recruited macrophages distinct from kupffer cells in the fatty liver. *Immunity* **53**, 641–657.e14 (2020).
15. N. Joshi, S. Watanabe, R. Verma, R. P. Jablonski, C. I. Chen, P. Cheresh, N. S. Markov, P. A. Reyfman, A. C. McQuattie-Pimentel, L. Sichizya, Z. Lu, R. Piseaux-Aillon, D. Kirchenbuechler, A. S. Flozak, C. J. Gottardi, C. M. Cuda, H. Perlman, M. Jain, D. W. Kamp, G. R. S. Budinger, A. V. Misharin, A spatially restricted fibrotic niche in pulmonary fibrosis is sustained by M-CSF/M-CSFR signalling in monocyte-derived alveolar macrophages. *Eur. Respir. J.* **55**, 1900646 (2020).
16. P. A. Reyfman, J. M. Walter, N. Joshi, K. R. Anekalla, A. C. McQuattie-Pimentel, S. Chiu, R. Fernandez, M. Akbarpour, C. I. Chen, Z. Ren, R. Verma, H. Abdala-Valencia, K. Nam, M. Chi, S. Han, F. J. Gonzalez-Gonzalez, S. Soberanes, S. Watanabe, K. J. N. Williams, A. S. Flozak, T. T. Nicholson, V. K. Morgan, D. R. Winter, M. Hinchcliff, C. L. Hrusch, R. D. Guzy, C. A. Bonham, A. I. Sperling, R. Bag, R. B. Hamanaka, G. M. Mutlu, A. V. Yeldandi, S. A. Marshall, A. Shilatifard, L. A. N. Amaral, H. Perlman, J. I. Sznajder, A. C. Argento,

Downloaded from https://www.science.org at Tsinghua University on October 24, 2025

C. T. Gillespie, J. Dematte, M. Jain, B. D. Singer, K. M. Ridge, A. P. Lam, A. Bharat, S. M. Bhorade, C. J. Gottardi, G. R. S. Budinger, A. V. Misharin, Single-cell transcriptomic analysis of human lung provides insights into the pathobiology of pulmonary fibrosis. *Am. J. Respir. Crit. Care Med.* **199**, 1517–1536 (2019).

17. T. S. Adams, J. C. Schupp, S. Poli, E. A. Ayaub, N. Neumark, F. Ahangari, S. G. Chu, B. A. Raby, G. Deluliis, M. Januszyk, Q. Duan, H. A. Arnett, A. Siddiqui, G. R. Washko, R. Homer, X. Yan, I. O. Rosas, N. Kaminski, Single-cell RNA-seq reveals ectopic and aberrant lung-resident cell populations in idiopathic pulmonary fibrosis. *Sci. Adv.* **6**, eaba1983 (2020).
18. C. Morse, T. Tabib, J. Sembrat, K. L. Buschur, H. T. Bittar, E. Valenzi, Y. Jiang, D. J. Kass, K. Gibson, W. Chen, A. Mora, P. V. Benos, M. Rojas, R. Lafyatis, Proliferating SPP1/MERTK-expressing macrophages in idiopathic pulmonary fibrosis. *Eur. Respir. J.* **54**, 1802441 (2019).
19. J. Hou, J. Zhang, P. Cui, Y. Zhou, C. Liu, X. Wu, Y. Ji, S. Wang, B. Cheng, H. Ye, L. Shu, K. Zhang, D. Wang, J. Xu, Q. Shu, M. Colonna, X. Fang, TREM2 sustains macrophage-hepatocyte metabolic coordination in nonalcoholic fatty liver disease and sepsis. *J. Clin. Invest.* **131**, e135197 (2021).
20. S. Daemen, A. Gainullina, G. Kalugotla, L. He, M. M. Chan, J. W. Beals, K. H. Liss, S. Klein, A. E. Feldstein, B. N. Finck, M. N. Artyomov, J. D. Schilling, Dynamic shifts in the composition of resident and recruited macrophages influence tissue remodeling in NASH. *Cell Rep.* **34**, 108626 (2021).
21. D. A. Jaitin, L. Adlung, C. A. Thaiss, A. Weiner, B. Li, H. Descamps, P. Lundgren, C. Bleriot, Z. Liu, A. Deczkowska, H. Keren-Shaul, E. David, N. Zmora, S. M. Eldar, N. Lubezky, O. Shibolet, D. A. Hill, M. A. Lazar, M. Colonna, F. Ginhoux, H. Shapiro, E. Elinav, I. Amit, Lipid-associated macrophages control metabolic homeostasis in a Trem2-dependent manner. *Cell* **178**, 686–698.e14 (2019).
22. C. Cochain, E. Vafadarnejad, P. Arampatzi, J. Pelisek, H. Winkels, K. Ley, D. Wolf, A. E. Saliba, A. Zernecke, Single-cell RNA-seq reveals the transcriptional landscape and heterogeneity of aortic macrophages in murine atherosclerosis. *Circ. Res.* **122**, 1661–1674 (2018).
23. H. Keren-Shaul, A. Spinrad, A. Weiner, O. Matcovitch-Natan, R. Dvir-Szternfeld, T. K. Ulland, E. David, K. Baruch, D. Lara-Astaiso, B. Toth, S. Itzkovitz, M. Colonna, M. Schwartz, I. Amit, A unique microglia type associated with restricting development of Alzheimer's disease. *Cell* **169**, 1276–1290.e17 (2017).
24. A. A. Nugent, K. Lin, B. van Lengerich, S. Lianoglou, L. Przybyla, S. S. Davis, C. Llapashtica, J. Wang, D. J. Kim, D. Xia, A. Lucas, S. Baskaran, P. C. G. Haddick, M. Lenser, T. K. Earr, J. Shi, J. C. Dugas, B. J. Andreone, T. Logan, H. O. Solanoy, H. Chen, A. Srivastava, S. B. Poda, P. E. Sanchez, R. J. Watts, T. Sandmann, G. Astarita, J. W. Lewcock, K. M. Monroe, G. Di Paolo, TREM2 regulates microglial cholesterol metabolism upon chronic phagocytic challenge. *Neuron* **105**, 837–854.e9 (2020).
25. W. Z. Mehal, J. Iredale, S. L. Friedman, Scraping fibrosis: Expressway to the core of fibrosis. *Nat. Med.* **17**, 552–553 (2011).
26. A. V. Misharin, L. Morales-Nebreda, P. A. Reyfman, C. M. Cuda, J. M. Walter, A. C. McQuattie-Pimentel, C. I. Chen, K. R. Anekalla, N. Joshi, K. J. N. Williams, H. Abdala-Valencia, T. J. Yacoub, M. Chi, S. Chiu, F. J. Gonzalez-Gonzalez, K. Gates, A. P. Lam, T. T. Nicholson, P. J. Homan, S. Soberanes, S. Dominguez, V. K. Morgan, R. Saber, A. Shaffer, M. Hinchcliff, S. A. Marshall, A. Bharat, S. Berdnikovs, S. M. Bhorade, E. T. Bartom, R. I. Morimoto, W. E. Balch, J. I. Sznajder, N. S. Chandel, G. M. Mutlu, M. Jain, C. J. Gottardi, B. D. Singer, K. M. Ridge, N. Bagheri, A. Shilatifard, G. R. S. Budinger, H. Perlman, Monocyte-derived alveolar macrophages drive lung fibrosis and persist in the lung over the life span. *J. Exp. Med.* **214**, 2387–2404 (2017).
27. M. Guilliams, G. R. Thierry, J. Bonnardel, M. Bajenoff, Establishment and maintenance of the macrophage niche. *Immunity* **52**, 434–451 (2020).
28. T. Hendrikx, F. Porsch, M. G. Kiss, D. Rajcic, N. Papac-Miličević, C. Hoebinger, L. Goederle, A. Hladik, L. E. Shaw, H. Horstmann, S. Knapp, S. Derdak, M. Bilban, L. Heintz, M. Krawczyk, R. Paternostro, M. Trauner, M. Farlik, D. Wolf, C. J. Binder, Soluble TREM2 levels reflect the recruitment and expansion of TREM2$^+$ macrophages that localize to fibrotic areas and limit NASH. *J. Hepatol.* **77**, 1373–1385 (2022).
29. M. J. Perugorria, A. Esparza-Baquer, F. Oakley, I. Labiano, A. Korosec, A. Jais, J. Mann, D. Tiniakos, A. Santos-Laso, A. Arbelaiz, R. Gawish, A. Sampedro, A. Fontanellas, E. Hijona, R. Jimenez-Agüero, H. Esterbauer, D. Stoiber, L. Bujanda, J. M. Banales, S. Knapp, O. Sharif, D. A. Mann, Non-parenchymal TREM-2 protects the liver from immune-mediated hepatocellular damage. *Gut* **68**, 533–546 (2019).
30. I. Labiano, A. Agirre-Lizaso, P. Olaizola, A. Echebarria, M. Huici-Izagirre, I. Olaizola, A. Esparza-Baquer, O. Sharif, E. Hijona, P. Milkiewicz, M. Milkiewicz, F. González-Romero, P. Aspichueta, M. J. Monte, J. J. G. Marin, M. Vucur, T. Luedde, M. Marzioni, D. A. Mann, L. Bujanda, P. M. Rodrigues, J. M. Banales, M. J. Perugorria, TREM-2 plays a protective role in cholestasis by acting as a negative regulator of inflammation. *J. Hepatol.* **77**, 991–1004 (2022).
31. A. Esparza-Baquer, I. Labiano, O. Sharif, A. Agirre-Lizaso, F. Oakley, P. M. Rodrigues, E. Zhuravleva, C. J. O'Rourke, E. Hijona, R. Jimenez-Agüero, I. Riaño, A. Landa, A. La Casta, M. Y. W. Zaki, P. Munoz-Garrido, M. Azkargorta, F. Elortza, A. Vogel, G. Schabbauer, P. Aspichueta, J. B. Andersen, S. Knapp, D. A. Mann, L. Bujanda, J. M. Banales, M. J. Perugorria, TREM-2 defends the liver against hepatocellular carcinoma through multifactorial protective mechanisms. *Gut* **70**, 1345–1361 (2021).
32. S. A. Park, M. J. Kim, S. Y. Park, J. S. Kim, W. Lim, J. S. Nam, Y. Yhong Sheen, TIMP-1 mediates TGF-β-dependent crosstalk between hepatic stellate and cancer cells via FAK signaling. *Sci. Rep.* **5**, 16492 (2015).
33. I. Tuominen, B. K. Fuqua, C. Pan, N. Renaud, K. Wroblewski, M. Civelek, K. Clerkin, A. Asaryan, S. G. Haroutunian, J. Loureiro, J. Borawski, G. Roma, J. Knehr, W. Carbone, S. French, B. W. Parks, S. T. Hui, M. Mehrabian, C. Magyar, R. M. Cantor, C. Ukomadu, A. J. Lusis, S. W. Beaven, The genetic architecture of carbon tetrachloride-induced liver fibrosis in mice. *Cell. Mol. Gastroenterol. Hepatol.* **11**, 199–220 (2021).
34. K. Kumagai, K. Tabu, F. Sasaki, Y. Takami, Y. Morinaga, S. Mawatari, S. Hashimoto, S. Tanoue, S. Kanmura, T. Tamai, A. Moriuchi, H. Uto, H. Tsubouchi, A. Ido, Glycoprotein nonmetastatic melanoma B (Gpnmb)-positive macrophages contribute to the balance between fibrosis and fibrolysis during the repair of acute liver injury in mice. *PLOS ONE* **10**, e0143413 (2015).
35. B. Li, J. M. Reynolds, R. D. Stout, D. A. Bernlohr, J. Suttles, Regulation of Th17 differentiation by epidermal fatty acid-binding protein. *J. Immunol.* **182**, 7625–7633 (2009).
36. M. Shan, X. Yuan, L. Z. Song, L. Roberts, N. Zarinkamar, A. Seryshev, Y. Zhang, S. Hilsenbeck, S. H. Chang, C. Dong, D. B. Corry, F. Kheradmand, Cigarette smoke induction of osteopontin (SPP1) mediates T_H17 inflammation in human and experimental emphysema. *Sci. Transl. Med.* **4**, 117ra119 (2012).
37. T. Kobayashi, H. Kim, X. Liu, H. Sugiura, T. Kohyama, Q. Fang, F. Q. Wen, S. Abe, X. Wang, J. J. Atkinson, J. M. Shipley, R. M. Senior, S. I. Rennard, Matrix metalloproteinase-9 activates TGF-β and stimulates fibroblast contraction of collagen gels. *Am. J. Physiol. Lung Cell. Mol. Physiol.* **306**, L1006–L1015 (2014).
38. S. A. MacParland, J. C. Liu, X. Z. Ma, B. T. Innes, A. M. Bartczak, B. K. Gage, J. Manuel, N. Khuu, J. Echeverri, I. Linares, R. Gupta, M. L. Cheng, L. Y. Liu, D. Camat, S. W. Chung, R. K. Seliga, Z. Shao, E. Lee, S. Ogawa, M. Ogawa, M. D. Wilson, J. E. Fish, M. Selzner, A. Ghanekar, D. Grant, P. Greig, G. Sapisochin, N. Selzner, N. Winegarden, O. Adeyi, G. Keller, G. D. Bader, I. D. McGilvray, Single cell RNA sequencing of human liver reveals distinct intrahepatic macrophage populations. *Nat. Commun.* **9**, 4383 (2018).
39. T. S. Andrews, J. Atif, J. C. Liu, C. T. Perciani, X. Z. Ma, C. Thoeni, M. Slyper, G. Eraslan, A. Segerstolpe, J. Manuel, S. Chung, E. Winter, I. Cirlan, N. Khuu, S. Fischer, O. Rozenblatt-Rosen, A. Regev, I. D. McGilvray, G. D. Bader, S. A. MacParland, Single-cell, single-nucleus, and spatial RNA sequencing of the human liver identifies cholangiocyte and mesenchymal heterogeneity. *Hepatol. Commun.* **6**, 821–840 (2022).
40. J. Zhao, S. Zhang, Y. Liu, X. He, M. Qu, G. Xu, H. Wang, M. Huang, J. Pan, Z. Liu, Z. Li, L. Liu, Z. Zhang, Single-cell RNA sequencing reveals the heterogeneity of liver-resident immune cells in human. *Cell Discov.* **6**, 22 (2020).
41. A. Sharma, J. J. W. Seow, C. A. Dutertre, R. Pai, C. Blériot, A. Mishra, R. M. M. Wong, G. S. N. Singh, S. Sudhagar, S. Khalilnezhad, S. Erdal, H. M. Teo, A. Khalilnezhad, S. Chakarov, T. K. H. Lim, A. C. Y. Fui, A. K. W. Chieh, C. P. Chung, G. K. Bonney, B. K. Goh, J. K. Y. Chan, P. K. H. Chow, F. Ginhoux, R. DasGupta, Onco-fetal reprogramming of endothelial cells drives immunosuppressive macrophages in hepatocellular carcinoma. *Cell* **183**, 377–394.e21 (2020).
42. M. Guilliams, J. Bonnardel, B. Haest, B. Vanderborght, C. Wagner, A. Remmerie, A. Bujko, L. Martens, T. Thoné, R. Browaeys, F. F. De Ponti, B. Vanneste, C. Zwicker, F. R. Svedberg, T. Vanhalewyn, A. Gonçalves, S. Lippens, B. Devriendt, E. Cox, G. Ferrero, V. Wittamer, A. Willaert, S. J. F. Kaptein, J. Neyts, K. Dallmeier, P. Geldhof, S. Casaert, B. Deplancke, P. Ten Dijke, A. Hoorens, A. Vanlander, F. Berrevoet, Y. Van Nieuwenhove, Y. Saeys, W. Saelens, H. Van Vlierberghe, L. Devisscher, C. L. Scott, Spatial proteogenomics reveals distinct and evolutionarily conserved hepatic macrophage niches. *Cell* **185**, 379–396.e38 (2022).
43. E. Valenzi, M. Bulik, T. Tabib, C. Morse, J. Sembrat, H. Trejo Bittar, M. Rojas, R. Lafyatis, Single-cell analysis reveals fibroblast heterogeneity and myofibroblasts in systemic sclerosis-associated interstitial lung disease. *Ann. Rheum. Dis.* **78**, 1379–1387 (2019).
44. A. C. Habermann, A. J. Gutierrez, L. T. Bui, S. L. Yahn, N. I. Winters, C. L. Calvi, L. Peter, M. I. Chung, C. J. Taylor, C. Jetter, L. Raju, J. Roberson, G. Ding, L. Wood, J. M. S. Sucre, B. W. Richmond, A. P. Serezani, W. J. McDonnell, S. B. Mallal, M. J. Bacchetta, J. E. Loyd, C. M. Shaver, L. B. Ware, R. Bremner, R. Walia, T. S. Blackwell, N. E. Banovich, J. A. Kropski, Single-cell RNA sequencing reveals profibrotic roles of distinct epithelial and mesenchymal lineages in pulmonary fibrosis. *Sci. Adv.* **6**, eaba1972 (2020).
45. T. Tsukui, K. H. Sun, J. B. Wetter, J. R. Wilson-Kanamori, L. A. Hazelwood, N. C. Henderson, T. S. Adams, J. C. Schupp, S. D. Poli, I. O. Rosas, N. Kaminski, M. A. Matthay, P. J. Wolters, D. Sheppard, Collagen-producing lung cell atlas identifies multiple subsets with distinct localization and relevance to fibrosis. *Nat. Commun.* **11**, 1920 (2020).
46. S. Durinck, P. T. Spellman, E. Birney, W. Huber, Mapping identifiers for the integration of genomic datasets with the R/bioconductor package biomaRt. *Nat. Protoc.* **4**, 1184–1191 (2009).
47. C. Hafemeister, R. Satija, Normalization and variance stabilization of single-cell RNA-seq data using regularized negative binomial regression. *Genome Biol.* **20**, 296 (2019).

Downloaded from https://www.science.org at Tsinghua University on October 24, 2025

48. I. Korsunsky, N. Millard, J. Fan, K. Slowikowski, F. Zhang, K. Wei, Y. Baglaenko, M. Brenner, P. R. Loh, S. Raychaudhuri, Fast, sensitive and accurate integration of single-cell data with Harmony. *Nat. Methods* **16**, 1289–1296 (2019).
49. M. F. Molina, T. Fabre, A. Cleret-Buhot, G. Soucy, L. Meunier, M. N. Abdelnabi, N. Belforte, S. Turcotte, N. H. Shoukry, Visualization, quantification, and mapping of immune cell populations in the tumor microenvironment. *J. Vis. Exp.* , e60740 (2020).
50. J. Schindelin, I. Arganda-Carreras, E. Frise, V. Kaynig, M. Longair, T. Pietzsch, S. Preibisch, C. Rueden, S. Saalfeld, B. Schmid, J. Y. Tinevez, D. J. White, V. Hartenstein, K. Eliceiri, P. Tomancak, A. Cardona, Fiji: An open-source platform for biological-image analysis. *Nat. Methods* **9**, 676–682 (2012).
51. R. Botvinik-Nezer, F. Holzmeister, C. F. Camerer, A. Dreber, J. Huber, M. Johannesson, M. Kirchler, R. Iwanir, J. A. Mumford, R. A. Adcock, P. Avesani, B. M. Baczkowski, A. Bajracharya, L. Bakst, S. Ball, M. Barilari, N. Bault, D. Beaton, J. Beitner, R. G. Benoit, R. Berkers, J. P. Bhanji, B. B. Biswal, S. Bobadilla-Suarez, T. Bortolini, K. L. Bottenhorn, A. Bowring, S. Braem, H. R. Brooks, E. G. Brudner, C. B. Calderon, J. A. Camilleri, J. J. Castrellon, L. Cecchetti, E. C. Cieslik, Z. J. Cole, O. Collignon, R. W. Cox, W. A. Cunningham, S. Czoschke, K. Dadi, C. P. Davis, A. Luca, M. R. Delgado, L. Demetriou, J. B. Dennison, X. Di, E. W. Dickie, E. Dobryakova, C. L. Donnat, J. Dukart, N. W. Duncan, J. Durnez, A. Eed, S. B. Eickhoff, A. Erhart, L. Fontanesi, G. M. Fricke, S. Fu, A. Galvan, R. Gau, S. Genon, T. Glatard, E. Glerean, J. J. Goeman, S. A. E. Golowin, C. Gonzalez-Garcia, K. J. Gorgolewski, C. L. Grady, M. A. Green, J. F. G. Moreira, O. Guest, S. Hakimi, J. P. Hamilton, R. Hancock, G. Handjaras, B. B. Harry, C. Hawco, P. Herholz, G. Herman, S. Heunis, F. Hoffstaedter, J. Hogeveen, S. Holmes, C. P. Hu, S. A. Huettel, M. E. Hughes, V. Iacovella, A. D. Iordan, P. M. Isager, A. I. Isik, A. Jahn, M. R. Johnson, T. Johnstone, M. J. E. Joseph, A. C. Juliano, J. W. Kable, M. Kassinopoulos, C. Koba, X. Z. Kong, T. R. Koscik, N. E. Kucukboyaci, B. A. Kuhl, S. Kupek, A. R. Laird, C. Lamm, R. Langner, N. Lauharatanahirun, H. Lee, S. Lee, A. Leemans, A. Leo, E. Lesage, F. Li, M. Y. C. Li, P. C. Lim, E. N. Lintz, S. W. Liphardt, A. B. L. Vermeer, B. C. Love, M. L. Mack, N. Malpica, T. Marins, C. Maumet, K. McDonald, J. T. McGuire, H. Melero, A. S. M. Leal, B. Meyer, K. N. Meyer, G. Mihai, G. D. Mitsis, J. Moll, D. M. Nielson, G. Nilsonne, M. P. Notter, E. Olivetti, A. I. Onicas, P. Papale, K. R. Patil, J. E. Peelle, A. Perez, D. Pischedda, J. B. Poline, Y. Prystauka, S. Ray, P. A. Reuter-Lorenz, R. C. Reynolds, E. Ricciardi, J. R. Rieck, A. M. Rodriguez-Thompson, A. Romyn, T. Salo, G. R. Samanez-Larkin, E. Sanz-Morales, M. L. Schlichting, D. H. Schultz, Q. Shen, M. A. Sheridan, J. A. Silvers, K. Skagerlund, A. Smith, D. V. Smith, P. Sokol-Hessner, S. R. Steinkamp, S. M. Tashjian, B. Thirion, J. N. Thorp, G. Tinghog, L. Tisdall, S. H. Tompson, C. Toro-Serey, J. J. T. Tresols, L. Tozzi, V. Truong, L. Turella, A. E. van't Veer, T. Verguts, J. M. Vettel, S. Vijayarajah, K. Vo, M. B. Wall, W. D. Weeda, S. Weis, D. J. White, D. Wisniewski, A. Xifra-Porxas, E. A. Yearling, S. Yoon, R. Yuan, K. S. L. Yuen, L. Zhang, X. Zhang, J. E. Zosky, T. E. Nichols, R. A. Poldrack, T. Schonberg, Variability in the analysis of a single neuroimaging dataset by many teams. *Nature* **582**, 84–88 (2020).
52. C. S. McGinnis, D. M. Patterson, J. Winkler, D. N. Conrad, M. Y. Hein, V. Srivastava, J. L. Hu, L. M. Murrow, J. S. Weissman, Z. Werb, E. D. Chow, Z. J. Gartner, MULTI-seq: Sample multiplexing for single-cell RNA sequencing using lipid-tagged indices. *Nat. Methods* **16**, 619–626 (2019).
53. D. M. Church, L. Goodstadt, L. W. Hillier, M. C. Zody, S. Goldstein, X. She, C. J. Bult, R. Agarwala, J. L. Cherry, M. DiCuccio, W. Hlavina, Y. Kapustin, P. Meric, D. Maglott, Z. Birtle, A. C. Marques, T. Graves, S. Zhou, B. Teague, K. Potamousis, C. Churas, M. Place, J. Herschleb, R. Runnheim, D. Forrest, J. Amos-Landgraf, D. C. Schwartz, Z. Cheng, K. Lindblad-Toh, E. E. Eichler, C. P. Ponting; The Mouse Genome Sequencing Consortium, Lineage-specific biology revealed by a finished genome assembly of the mouse. *PLOS Biol.* **7**, e1000112 (2009).
54. J. Jurka, Repbase update: A database and an electronic journal of repetitive elements. *Trends Genet.* **16**, 418–420 (2000).
55. G. La Manno, R. Soldatov, A. Zeisel, E. Braun, H. Hochgerner, V. Petukhov, K. Lidschreiber, M. E. Kastriti, P. Lonnerberg, A. Furlan, J. Fan, L. E. Borm, Z. Liu, D. van Bruggen, J. Guo, X. He, R. Barker, E. Sundstrom, G. Castelo-Branco, P. Cramer, I. Adameyko, S. Linnarsson, P. V. Kharchenko, RNA velocity of single cells. *Nature* **560**, 494–498 (2018).
56. R. Satija, J. A. Farrell, D. Gennert, A. F. Schier, A. Regev, Spatial reconstruction of single-cell gene expression data. *Nat. Biotechnol.* **33**, 495–502 (2015).
57. M. Stoeckius, S. Zheng, B. Houck-Loomis, S. Hao, B. Z. Yeung, W. M. Mauck III, P. Smibert, R. Satija, Cell Hashing with barcoded antibodies enables multiplexing and doublet detection for single cell genomics. *Genome Biol.* **19**, 224 (2018).
58. L. Zappia, A. Oshlack, Clustering trees: A visualization for evaluating clusterings at multiple resolutions. *Gigascience* **7**, giy083 (2018).
59. V. Bergen, M. Lange, S. Peidli, F. A. Wolf, F. J. Theis, Generalizing RNA velocity to transient cell states through dynamical modeling. *Nat. Biotechnol.* **38**, 1408–1414 (2020).
60. J. Alquicira-Hernandez, J. E. Powell, Nebulosa recovers single-cell gene expression signals by kernel density estimation. *Bioinformatics* **37**, 2485–2487 (2021).

Acknowledgments: We thank the Pfizer Flow Cytometry, Optical Microscopy, High Content Imaging, and Next-Generation Sequencing Technology Centers. T.F. and A.M.S.B. thank the Pfizer WRDM Postdoctoral Fellowship Program for prior support. **Funding:** This work was funded by Pfizer Inc. **Author contributions:** T.F., A.M.S.B., S.M.C., J.W., J.M., F.S., K.M.H., T.A.W., and K.D. conceptualized the study. T.F., A.M.S.B., and S.A. were responsible for the methodology. T.F., A.M.S.B., S.M.C., S.A., M.H.W., X.C., and M.P.L. conducted the formal analysis. T.F., A.M.S.B., J.W., J.M., F.S., A.W., and K.B. executed the investigational aspects of this study. Resources used in this study were contributed by J.W., J.M., F.S., K.M.K., A.J.F., L.A.B., and N.C.H. Data curation was performed by A.M.S.B., S.M.C., S.A., M.H.W., X.C., C.W. and K.M.K. Visualization of the data was executed by T.F., A.M.S.B., S.M.C., S.A., and M.H.W. Funding for this study was acquired by T.A.W. and K.D. The original draft of this manuscript was written by T.F., A.M.S.B., S.M.C., M.H.W., S.A., F.S., K.M.H., K.M.K., A.J.F., L.A.B., N.C.H., T.A.W., and K.D. Review and editing of the final manuscript were performed by T.F., A.M.S.B., S.M.C., K.M.H., T.A.W., and K.D. **Competing interests:** T.F., A.M.S.B., S.M.C., M.H.W., X.C., C.W., S.A., J.W., J.M., F.S., A.W., K.M.H., K.M.K., T.A.W., and K.D. are employees of Pfizer Inc. L.A.B. is a founder, shareholder, and director of FibroFind Ltd. N.C.H. has received research funding from AbbVie, Pfizer, Gilead, and Galecto, and is an advisor or consultant for Galecto, Indalo Therapeutics, Pliant Therapeutics, GSK, Boehringer-Ingelheim, Q32 Bio, and Ambys Medicines. **Data and materials availability:** All data needed to evaluate the conclusions in the paper are present in the paper or the Supplementary Materials with two exceptions. First, the human scRNA-seq data used in this study are available through NCBI using the accession numbers listed in Materials and Methods. Second, the murine scRNA-seq data generated for this study are available at the NCBI SRA under accession #GSE228232.

Submitted 15 July 2022
Accepted 16 March 2023
Published 7 April 2023
10.1126/sciimmunol.add8945

Downloaded from https://www.science.org at Tsinghua University on October 24, 2025